Mechanical Systems and Signal Processing 161 (2021) 107920

Contents lists available at ScienceDirect

Mechanical Systems and Signal Processing

journal homepage: www.elsevier.com/locate/ymssp

A probabilistic optimal sensor design approach for structural health monitoring using risk-weighted f-divergence

Yichao Yang [a], Mayank Chadha [a], Zhen Hu [b], Manuel A. Vega [a], Matthew D. Parno [c], Michael D. Todd [a,*]

[a] University of California San Diego, 9500 Gilman Drive, La Jolla, CA 92093-0085, USA
[b] University of Michigan-Dearborn, Dearborn, MI 48128, USA
[c] Cold Regions Research and Engineering Laboratory, Hanover, NH, USA

ARTICLE INFO

Article history:
Received 30 October 2020
Received in revised form 14 March 2021
Accepted 26 March 2021
Available online xxxx
Communicated by Spilios Fassois

Keywords:
Optimal sensor design
f-divergence
Risk
Bayesian inference
uncertainty quantification
Bayesian optimization
Miter gates

ABSTRACT

This paper presents a new approach to optimal sensor design for structural health monitoring (SHM) applications using a modified f-divergence objective functional. One of the primary goals of SHM is to infer the unknown and uncertain damage state parameter(s) from the acquired data or features derived from the data. In this work, we consider the loss of boundary contact (a "gap") between a navigation lock miter gate and the supporting wall quoin block at the bottom of the gate to be the damage state parameter of concern. The design problem requires the optimal sensor placement of strain gages to obtain the best possible inference of the probability distribution of the gap length using the data from the multi-dimensional strain-gauge array. Using the notion of f-divergences (measures of difference between probability distributions), a risk-adjustment is made by using functions that weigh the importance of acquiring useful information for a given true value of the state-parameter and using Bayesian optimization. For this case study of miter gate monitoring, a computationally expensive high-fidelity finite element model and its digital surrogate is employed to provide efficient, previously-validated data.

1. Introduction

Structural health monitoring (SHM) is a multi-part paradigm that aims at assessing the state of the structural system and its ability to perform the desired design functionality by analyzing in-situ sensor measurement data. A well-designed SHM strategy enables the choice of optimal maintenance implementation, helps the structure achieve maximum performance, reduces ownership cost, minimizes unscheduled downtime, and potentially helps to avoid structural failures that can cause material or personal losses. Such an SHM system is desirable only if the benefits obtained from using the acquired information over the structure's life outweigh the cost of installing and maintaining that SHM system [1]. Hence, the value of an SHM system essentially depends on its design; at the core of any well-designed SHM system is a data acquisition system that relies on (usually an array of) deployed sensors to initiate the information workflow from which ultimate decisions about operations, maintenance, and other life cycle actions will be made. Therefore, the optimal design of this sensor network–defined herein as the spatial arrangement of the sensor network–can significantly enhance the performance and life cycle value

* Corresponding author.
E-mail addresses: yiy018@ucsd.edu (Y. Yang), machadha@ucsd.edu (M. Chadha), zhennhu@umich.edu (Z. Hu), mvegaloo@ucsd.edu (M.A. Vega), matthew.d.parno@erdc.dren.mil (M.D. Parno), mdtodd@eng.ucsd.edu (M.D. Todd).

https://doi.org/10.1016/j.ymssp.2021.107920
0888-3270/

of the SHM system as a whole. Formulating and solving such an optimization problem is the central goal of this paper. Of course, other design parameters (beyond spatial arrangements such as data acquisition rate or duty cycle) or constraints (such as power availability) will also play a role in any specific application, but such multi-objective don't fundamentally alter the ideas presented in this work.

Due to the many sources of variability and noises in any SHM system's observations, the SHM process contains inherent uncertainties that need to be considered. The optimal sensor placement problem, therefore, aims to find a sensor configuration that gathers the information most useful for detecting the target state(s) subject to uncertainty [2,3]. The key element to this is the optimality criterion or objective function that is used to evaluate design utility. However, there is not a universal objective for sensor design, as each application has a distinct goal for the use of a particular SHM system. Consequently, different objective functions have been proposed in the past for optimal sensor placement design, starting with mode identification and correlation in some of the original works in this area, which were not necessarily SHM applications [4–8]. For example, in Ref. [4,8], the optimal sensor arrangement minimized the condition number of the Fisher information matrix corresponding to the target modes of dynamical structures. Sun et al. [9] proposed optimal sensor design by maximizing dynamic information of the structure using a limited number of sensors and proposed an artificial bee colony algorithm to solve the optimization problem. Austin et al. [10] used objective function formulated to reduce the type I and II errors and used adaptive mutation-based genetic algorithm for the sensor design. Similarly, Papadimitriou et al. [11] proposed minimizing entropy focusing on structural modal updating. In one of the first SHM-focused studies, Udwadia [12] and Basseville [13] have also used the Fisher information matrix to maximize the performance of SHM for structural modal identification. For some other application domains such as the aviation sector, decision-makers are more concerned with detecting outlier states of the structure, since the cost of failure is catastrophic [14]. Such maximization of outlier state detection has led to objective functions such as the probability of detection (POD), probability of classification [15], and the Mahalanobis distance measure [16]. There are several other seminal contributions in optimal sensor placement design for a wide class of SHM applications found in Refs. [17–19].

Given that decision-makers are the typical curators of SHM utility, the objective function may also be defined from the perspective of decision theory that defines *loss as a consequence of decision-making* (or the associated risk) by considering various prior information and uncertainty sources in the decision-making process. The loss/risk is a subjective quantity and is defined according to the problem. Optimal sensor design therein requires finding the sensor network that minimizes the losses or risk expressed by an objective function in an *average* sense; such an objective function is defined as *Bayes risk*. This is a more general definition of traditional Bayes risk, and it expands its applicability from a pure monetary-based standpoint to a more general optimization problem in the sense that risk is no longer confined to the likelihood of losing money, but rather can be thought of as a regret of making an undesirable decision or predicting undesirable outcomes. One such Bayes risk objective function for sensor placement design was developed by Flynn and Todd [20,21], in which Bayesian experimental design [22] is used for optimal sensor placement design by minimizing an appropriate Bayes risk functional. It was demonstrated in an ultrasonic guided wave sensor design problem that Bayes risk can minimize the total presence of either type I or type II decision errors in SHM. The use of expected Kullback–Leibler (K-L) divergence or expected utility in sensor placement design [23–25] can also be classified as a type of Bayes risk. While the idea of minimizing expected risk (or maximizing the utility of your desired outcome) using Bayes risk is powerful for optimizing sensor placement under uncertainty, its advantageously generic nature and currently unexploited benefits must be carefully considered. First, we note that the term risk is subjective and is somewhat open-ended to a desirable definition. The risk function or utility function can be formulated differently and will lead to different sensor placement designs, i.e., no utility function is generic to all problems. Second, current Bayes risk-type objective functions are incapable of incorporating human psychology or risk-perception of decision-makers in sensor network design.

Using the monitoring of lock navigation gates as an application case, this paper aims to address the two issues outlined above by expanding on the idea of Bayes risk-type objective functions to simultaneously evaluate the gain in information and consider the risk-perception of decision-makers in sensor network design. This is done by proposing a risk-weighted f-divergence functional for sensor placement design. Firstly, we investigate different types of f-divergence measures to evaluate the information gain of a particular sensor network design. Since the f-divergence gives a generic form to evaluate the distance (depicting gain information or *information divergence*) between two probability distribution functions, using different types of f-divergence helps to investigate and compare the effects of using different distance measures in the sensor placement optimization process. Secondly, the f-divergence is weighed with a risk-based weight function to incorporate a decision-maker's risk perception into sensor placement design. The f-divergence is modified using weight functions that weigh in the importance of acquiring good information for a given true value of the structural damage state. Thirdly, the f-divergence is also weighted by prior knowledge of the structural damage state. The proposed objective function in this paper is, therefore, the integral of the weighted f-divergence of the posterior distribution relative to the prior distribution, weighted over the prior distribution, and risk-based weight function, integrated over all the physically possible values of the structural damage states. The goal is to obtain the sensor network that maximizes the objective function (or maximizing the gain in the additional information or minimizing the risk or regret of inferring meaningless information regarding the damage states). The paper also proposes two different approaches to incorporate the risk weights into the Bayes risk functional. In the first approach, the risk-weights are included explicitly inside the integrand of the Bayes risk functional, whereas in the second approach, the risk weights are used to modify the prior damage distribution. Although mathematically equivalent, numerical evaluation of risk-weighted Bayes risk yields slightly different results.

In addition to the objective function, another long-standing challenge in sensor placement design is how to effectively and efficiently solve the posed optimization model. A common approach to optimization is iteratively searching for the optimal value guided by the steepest gradient descent. This approach has been used in machine-learning [26] and in developing an optimal sensor network [27]. For example, Akbarzadeh [2] used a gradient descent algorithm in sensor optimization by deriving derivatives at each step, which requires less computational effort. However, in many problems, the exact analytical derivatives are not available. Heuristic algorithms have also been widely used in the literature; for example, Jin [28] used a genetic algorithm to minimize the communication distance of sensors, while Yi et al. [29] utilized a genetic algorithm to obtain optimal sensor placement for a high-rise building monitoring system. However, the main drawback of these optimization strategies is that they must evaluate many samples, yielding a computationally expensive path to the solution. In complex large-scale SHM applications such as the civil infrastructure problems considered in this paper, the sensor design space itself is potentially prohibitively large, and this is coupled with the fact that obtaining and evaluating Bayes risk even once may require tens of thousands of runs of expensive simulations (such as if a finite element is used). This paper also proposes a novel numerical framework that seamlessly synthesizes Gaussian process regression [30], dimension reduction techniques [31,32], Bayesian optimization [33,34], and sequential Monte Carlo to break this computational challenge. In the proposed framework, once the desirable sensor measurements are obtained in one iteration of the optimization, the predictive model need not be run in order to evaluate the observed sensor measurements at every optimization iteration. As shown in the result section, this significantly improves the computational efficiency of the sensor placement design optimization and allows for a reduction of computational time from years to hours. The review papers [35–37] and the references therein serve as an excellent source of information on the optimal sensor network design and the computational methods to solve the optimization problems.

The proposed risk-weighted f-divergence functional and the efficient numerical framework to overcome the computational burden for sensor placement design will be demonstrated in a lock miter gate monitoring application. The United States Army Corps of Engineers (USACE) spends billions of dollars in maintaining and operating the USA's inland waterways navigation corridor, where the unscheduled shutdown of these assets and dewatering for inspection or repair is very costly [3,38,39]. Within the navigation corridor, miter gates are one of the most common types of lock gates employed [40]. Many of these structures have been operational for over 50 years, and without knowledge of their actual structural residual strength capacity, they could potentially be operating with a higher risk of failure. Current practice involves engineering elicitation via inspection, followed by lock closures if the inspection so warrants. Since this process is based on the varied experience and interpretation of field inspectors, it bears high uncertainty and variability [41], and USACE is investigating the use of SHM to potentially reduce those uncertainties. In general terms, the first step of the SHM system design is to decide what sensors are most suitable (e.g., discrete or continuous strain-gauges [42], accelerometers, etc.) to provide measurements that are most correlated to the type of damage or state to be inferred. The second step is then to obtain a sensor network design (e.g., number of sensors, location/-placement, duty cycle, etc.) that provides the most valuable information at a minimal cost [43,44], as broadly elucidated above. To this goal, in this paper, an optimal sensor network will be designed for a miter gate using the proposed framework.

The primary contributions of this paper may therefore be summarized as: (1) it proposes a risk-weighted f-divergence Bayes risk for sensor placement design and two different approaches to incorporate the risk weights into the Bayes risk functional; (2) it investigates and compares different types of f-divergence measures in the objective functional for sensor placement design; (3) it proposes a novel numerical framework that drastically reduces the required computational effort in sensor placement design by integrating Bayesian optimization, surrogate modeling, univariate dimensional reduction, and Sequential Monte Carlo; and (4) it demonstrates the proposed framework in a complex and practical miter gate monitoring application.

The rest of the paper is arranged as follows. Section 2 details the background of the miter gate SHM application and briefly discusses the proposed sensor placement design optimization framework. Section 3 details the associated Bayes risk functional, followed by Section 4 that investigates univariate dimensional reduction with Gauss-Hermite quadrature approach to evaluate the Bayes risk. Section 5 discusses the optimal sensor placement design using Bayesian optimization in detail and presents the novel algorithm used to overcome the computational burden. After a general discussion on Bayesian optimization, the remaining part of Section 5 discusses numerical results. Finally, Section 6 concludes the paper.

2. Problem description

Some preliminary definitions and notations are first necessary. The real number space in d dimension is represented by $\mathbb{R}^d$, with $\mathbb{R}^1 \equiv \mathbb{R}$. A random variable X is a real-valued function defined on a discrete or a continuous sample space S_X and is assumed to take values in a measurement space $\Omega_X \in \mathbb{R}^d$, such that $X : S_X \longrightarrow \Omega_X \in \mathbb{R}^d$. Lower case letters x represent realizations of the random variable X, such that $x \in \Omega_X$. The probability density function and the cumulative density function are represented by $f_X(x)$ and $F_X(x)$. The expected value of a function $g(x)$ is denoted by $E_X[g(x)]$. Lastly, a random variable X following a Gaussian distribution, with the mean μ_x and standard deviation σ_x is denoted by:

$$\begin{aligned} &f_X(x) = \tfrac{1}{\sigma_x}\phi\left(\tfrac{x-\mu_x}{\sigma_x}\right);\\ &F_X(x) = \Phi\left(\tfrac{x-\mu_x}{\sigma_x}\right);\\ &X \sim N(\mu_x, \sigma_x^2). \end{aligned} \tag{1}$$

No symbolic distinction is made for different dimensions d of the measurement space and the random variable. The vector-dimensionality of a random variable is contextual and is defined as needed.

Finally, let Ω_E represent the exhaustive sensor design space and $e \in \Omega_E$ represent a design realization. Let $\mathfrak{E}(e) : \Omega_E \longrightarrow \mathbb{R}$ denote the Bayes risk functional. The goals of this paper are: (1) to appropriately define the Bayes risk $\mathfrak{E}(e)$; (2) to devise a computationally-efficient approach to numerically evaluate the value of Bayes risk for a given design e; (3) to arrive at the most optimal design $e^* \in \Omega_E$, such that:

$$e^* = \text{argmax}_{e \in \Omega_E} \mathfrak{E}(e). \tag{2}$$

Evaluating the Bayes risk would require observable strain data under various damage scenarios. The sensor data is obtained using a validated finite element model. Therefore, the Bayes risk $\mathfrak{E}(e)$ and the design space Ω_E will both depend on a finite element model capable of estimating observable strains under various damage scenarios.

2.1. Miter gate: finite element model

The Greenup miter gate, which is maintained and managed by USACE on the Ohio River in the USA, is considered for a case study. Fig. 1 shows the Greenup lock and the miter gate (image adapted from the USACE website and Eick et al. [45]). Loss of contact in the quoin blocks is the most commonly observed damage mode in such systems [39,41,40]. Loss of contact leads to a formation of a very thin gap between the gate and the wall quoin blocks at the bottom of the gate, which induces undesirable load redistribution in the system. The length of the of loss of contact at the bottom of the gate is referred to as *gap length* in this paper; therefore, the gap length is considered as the continuous state-parameter $\theta \in \Omega_\Theta$ (refer to Fig. 2), such that $\Omega_\Theta = [\theta_{\text{low}}, \theta_{\text{up}}]$. Here, θ_{low} is the lower bound of the gap length defining the existence of "damage", and θ_{up} is the upper bound of the gap length defining critical damage of failure. This value is suggested by the USACE engineers based on their experience, past inspection data, or numerical simulation. In most cases, data related to the failure of the structure may not be available because decision-makers are risk-averse and prevent the gap length from approaching failure levels. In such scenarios, a rigorous high-fidelity numerical simulation should be performed to estimate the θ_{up}. Based on feedback from the field-engineers [40], the upper bound of the gap length can be considered as $\theta_{\text{up}} = 180$ inches for gates that have similar structural characteristics as the Greenup miter gate. If no value of θ_{low} is specified, it can be taken as 0 inch (indicating pristine state of the gate).

The loss-of-contact part of the gate is always submerged in highly turbid water, and it consequently cannot be easily measured directly during normal operational conditions. Hence, gap length is an unknown parameter and must be inferred from indirect measurements. The Greenup miter gate is equipped with a strain gauge network that records the operational strain measurements in real-time and will be used to infer the gap length. The data acquisition process is simulated using a high-fidelity finite element model (FEM) of the Greenup miter gate previously validated in the undamaged condition with the available strain sensor readings [40]. When the miter gate is new and pristine, the gap length could reasonably be presumed to be zero. As with any such model, its representative predictive value is only as good as its validation with regard to the real structure that it is modeling. In this case, the FEM was validated in the undamaged condition, but modeling of the damage itself could not be validated on actual data from the gate in a known damaged condition, so modeling bias in the damage state could exist. That does not invalidate the demonstration of the proposed approach or its utility but provides caution on interpreting the specific results for this case beyond the demonstration of the overall optimal sensor placement approach. With that caveat, the FEM will serve as the fundamental physical model for this study.

To arrive at the optimal sensor placement design, we rely on the validated finite element model to obtain the observable strain values. A sensor-network can be designed by picking strain gauges from a countable set of strain-locations where we

Fig. 1. Greenup locks and miter gate.

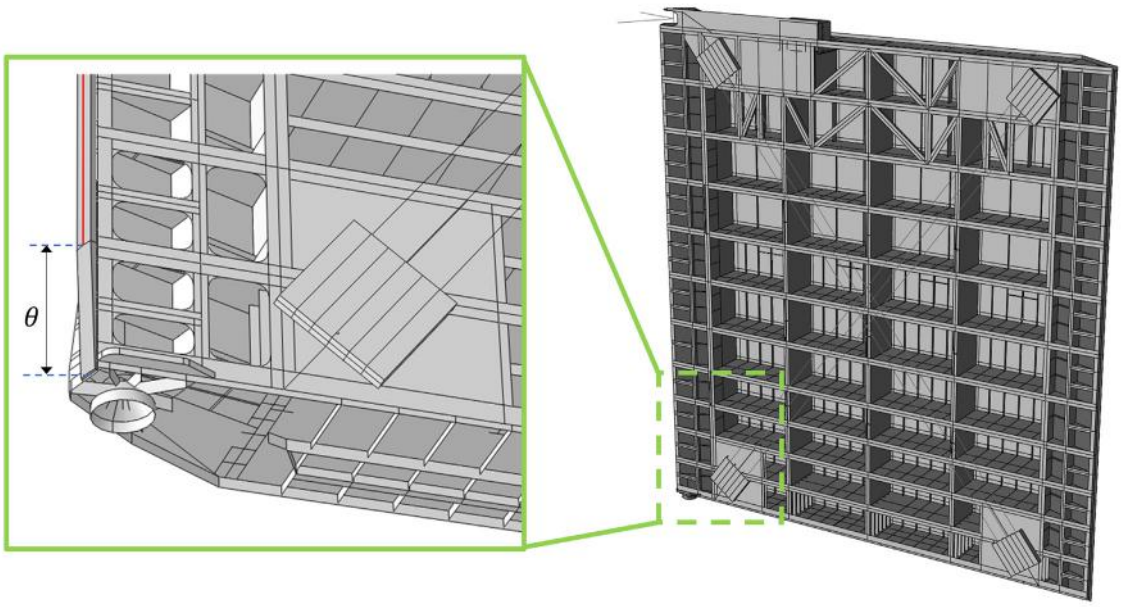

Fig. 2. Physics-based model of miter gate and the bearing gap.

have observable strain data for different damage scenarios. In our case, it is a set of 64919×4 strain locations as discussed later. Although there are infinite possible locations where strain gauges can be placed on a real miter gate, the finite element model discretely covers the possible sensor locations using a countable number of strain gauges. The finite element modeling itself is constructed using 3D quadrilateral and triangular shell elements in ABAQUS and consists of a total of 64919 elements. Every element has a local coordinate system $\{d_i\}$ defined in the undeformed state, and a global coordinate system $\{E_i\}$. The thickness of the element is in the direction d_3, and the top and bottom surface of the element is spanned by the vectors $(d_1 - d_2)$ as shown in Fig. 3. The strain gauges are attached to the top and bottom surface of each element, measuring uniaxial strains along the direction d_1 and d_2. Each element is identified by its geometric centroid at the origin of the local coordinate system. Therefore, there are four possible arrangements of strain gauges on each element. These possibilities are identified using the following abbreviations:

$$\begin{aligned}
&\text{TH : top element, horizontal orientation along } d_1;\\
&\text{TV : top element, vertical orientation along } d_2;\\
&\text{BH : bottom element, horizontal orientation along } d_1;\\
&\text{BV : bottom element, vertical orientation along } d_2.
\end{aligned} \tag{3}$$

Based on the above abbreviations, for a typical element m, x^m_{TH} and x^m_{TV} represent the measurement of strain from gauges attached to the top surface and oriented along d_1 and d_2, respectively. Similarly, x^m_{BH} and x^m_{BV} represent the measurements of strain from gauges attached to the bottom surface and oriented along d_1 and d_2, respectively. Therefore, any element m has four candidate strain gauges attached to it, whose readings are represented by a four-dimensional vector $x^m = (x^m_{\text{TH}}, x^m_{\text{TV}}, x^m_{\text{BH}}, x^m_{\text{BV}})$. Hence, there is a total of 64919×4 strain locations to be considered for optimal sensor design.

The gate is subjected to uncertain upstream and downstream hydrostatic loads quantified by the hydrostatic upstream and downstream heads; these are denoted by the random variables H_{up} and H_{down}, with realizations $h_{\text{up}} \in \Omega_{h_{\text{up}}}$ and $h_{\text{down}} \in \Omega_{h_{\text{down}}}$, respectively, where $\Omega_{H_{\text{up}}}$ and $\Omega_{H_{\text{down}}}$ represent the space of all possible values of upstream and downstream head, respectively. The water heads are modeled by a Gaussian distribution with their mean and variance reasonably assumed as

$$h_{\text{up}} \sim N\left(552\,\text{in}, 10^2\,\text{in}^2\right); \tag{4a}$$

$$h_{\text{down}} \sim N\left(168\,\text{in}, 20^2\,\text{in}^2\right). \tag{4b}$$

Independent zero-mean additive Gaussian noise, denoted by a random variable ζ_i with the realization ε_i, is assumed for each strain gauge,

$$\zeta_i \sim N\left(\mu_{\varepsilon_i} = 0,\, \sigma^2_{\varepsilon_i}\right) \tag{5}$$

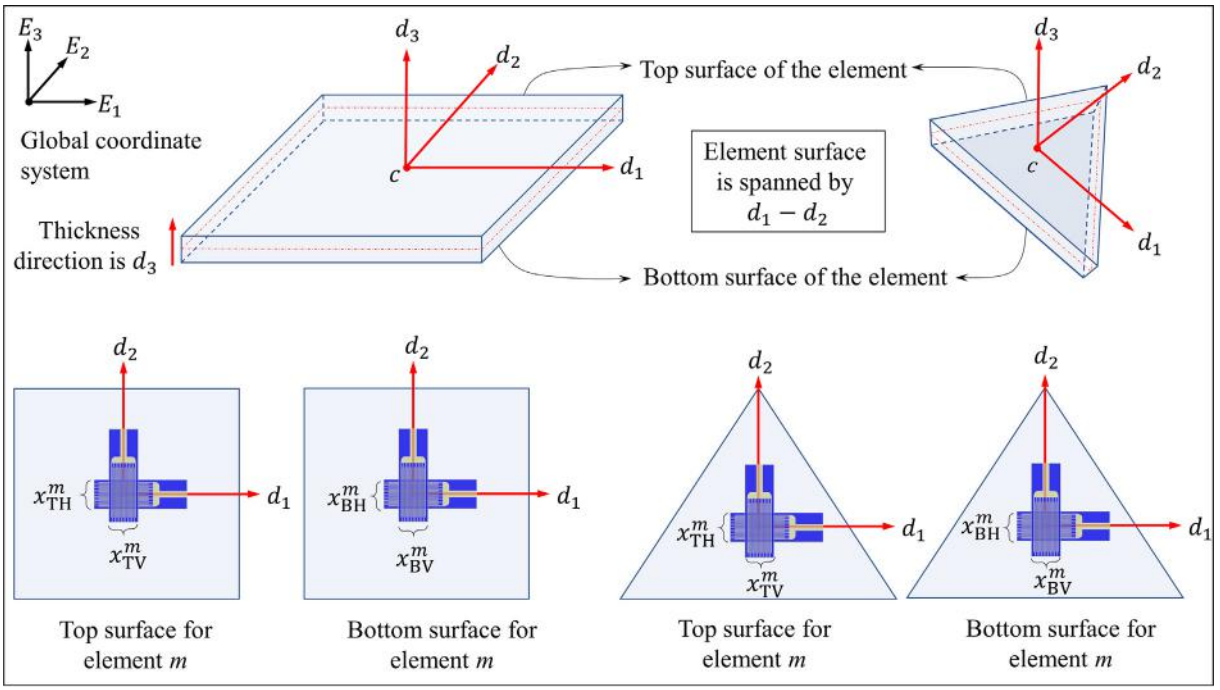

Fig. 3. Orientation and the location of the strain gauge and different type of shell elements used in FEM.

The value ε_i represents the realization of noise, and Ω_{ε_i} represents the noise space, such that $\varepsilon_i \in \Omega_{\varepsilon_i}$. The standard deviation of the noise is assigned to be $\sigma_{\varepsilon_i} = 5 \times 10^{-6}$ in accordance with reasonable commercial strain gauge performance.

The random nature of the water heads and strain gauge noise together make the observable strain values themselves random variables. Let $\Omega_X = \Omega_{X_{TH}} \cup \Omega_{X_{TV}} \cup \Omega_{X_{BH}} \cup \Omega_{X_{BV}}$ be the set of all the possible 64919×4 strain gauge locations. Here, $\Omega_{X_{TH}}$ and $\Omega_{X_{TV}}$ represents the space of all strain gauges attached to the top surface of element measuring strain in the direction d_1, and d_2 respectively. Similarly, $\Omega_{X_{BH}}$ and $\Omega_{X_{BV}}$ represents the space of all strain gauges attached to the bottom surface of element measuring strain in the direction d_1, and d_2 respectively. Let X denote the random vectors consisting of all strain measurements corresponding to Ω_X space, such that $x \in \Omega_X$ represent realizations of the random vectors X (see Eq. (9) for the relationship between the observed strain realization x, the strain output of FEM, and the noise in strain gauge). Finally, we denote the true values of the gap length, and hydrostatic heads as: $\theta_{\text{true}} \in \Omega_\theta, h_{\text{up-true}} \in \Omega_{H_{\text{up}}}, h_{\text{down-true}} \in \Omega_{H_{\text{down}}}$.

2.2. Miter gate: surrogate model

Solving the optimization problem posed in Eq. (2) requires evaluating the Bayes risk (defined later in Section (3) for various sensor network designs to arrive at an optimal design. As described below, each evaluation of the Bayes risk involves numerous FEM predictions to solve a Bayesian inference problem. This is computationally intractable and we seek computationally efficient approximations to the FEM. For Bayesian calibration, metamodels or surrogate models are preferable, e.g., Support Vector Regression (SVR) [46], Gaussian Process Regression (GPR) [46,34], Neural Network [47], and Polynomial Chaos Expansion (PCE) [48]. Some such approaches like SVR or neural networks yield point estimates/prediction, while others like GPR also predict the uncertainties associated with an average estimate/prediction. GPR is used to build a surrogate model in this work, which turns out to be 50,000 times faster than the FEM model. The output of the surrogate model still has a very large dimension; this is addressed using principal components analysis, which can be efficiently computed using the *singular value decomposition* (SVD) that reduces the high-dimensional, highly-correlated output space to low-dimensional, uncorrelated features. This is analogous to the "linear model of coregionalization" in the Gaussian process literature. Of the possible 64919×4 strain readings in Ω_X, 64919 strain measurements corresponding to each of the spaces $\Omega_{X_{TH}}, \Omega_{X_{TV}}, \Omega_{X_{BH}}$ and $\Omega_{X_{BV}}$ are considered independently. The 64919-dimensional strain response corresponding to each of the spaces $\Omega_{X_{TH}}, \Omega_{X_{TV}}, \Omega_{X_{BH}}$ and $\Omega_{X_{BV}}$ are transformed to lower 7, 12, 7, 12 feature spaces, respectively. Equivalently, the 64919×4-dimensional strain response corresponding to the spaces Ω_X are transformed to a lower 38 dimensional feature space that covers 95% of the total information of the strain data. We realize that the vertically oriented strain measurements have a larger number of features (12 features for both top and bottom strain gauges) than the horizontally oriented strain measurements (7 features for both top and bottom strain gauges). One possible reason is that the vertical strain responses are more sensitive to the dynamic loading considered in this paper (hydrostatic upstream and downstream loading) than

their counterparts in the horizontal direction, and hence require a larger number of features. Inversely, the larger number of features required to represent vertical strain gauge measurements also implies that the vertically oriented strain measurements have higher complexity (that by itself is a subjective quantity as described in [49]) than the horizontally oriented strain measurements. These 38 features can be inverted to obtain the complete strain gauge response. Four surrogate models for 7, 12, 7, 12 features corresponding to four strain measurement spaces $\Omega_{X_{\text{TH}}}, \Omega_{X_{\text{TV}}}, \Omega_{X_{\text{BH}}}$ and $\Omega_{X_{\text{BV}}}$ were built using GPR. We used a squared exponential kernel and we evaluated the hyper-parameters using maximum likelihood estimation. Since the GP models for each of these features were trained independently, they have different hyper-parameters. One-third of the 1000 data points were randomly used for training the GPR, and the remaining two-thirds were used for validation to verify the accuracy of the surrogate. Fig. 4 illustrates the discussion carried out so far. Like the FEM, the GPR model yields the 64919×4 dimensional strain response, but at a much cheaper computational cost.

2.3. Brief introduction to risk-weighted f-divergence based Bayesian optimization workflow for sensor placement design

Given the overall objective of an optimal sensing design, Ω_E represents the design space, such that $e \in \Omega_E$ represents a particular design realization. The design e consists of $N_{\text{sg}}(e)$ number of strain gauge measurement locations. Every design e yields different measurement data $x_e \in \Omega_{X_e}$. Here, $\Omega_{X_e} \subset \Omega_X$ represents the measurement space for the design e, and X_e denotes the corresponding random variable (see Eq. (10) that depicts how the observable strain realization x_e is obtained from the FEM and the strain gauge noise). Having defined the design space, four prominent steps are summarized below for the proposed risk-weighted f-divergence based Bayesian optimization framework for sensor network design.

2.3.1. Step 1: Problem description

This paper's objective could be phrased as attempting to answer the question: "Given sources of uncertainty (noise in the sensors and the uncertain external conditions), which set of sensors should be chosen among the possible 64919×4 strain gauges measurements that yields the maximum relative gain in the information contained in the posterior distribution of the target damage (gap length) relative to the information contained in the prior distribution?".

Consider a sensor network design $e \in \Omega_E$ with the measurement space Ω_{X_e}. Before any new/additional information is available about the structure through the strain gauge measurements, the uncertainty in the gap length is described by its prior probability distribution $f_\Theta(\theta)$. When additional information or strain gauge measurements are observed, it informs the observer (or the engineer) about the current state of the structure. This new information translates into the further refinement of the understanding of the gap length, now described by its posterior distribution $f_{\Theta|X_e}(\theta|x_e)$. If the strain gauge readings are representative of the true state of the structure, the posterior distribution $f_{\Theta|X_e}(\theta|x_e)$ draws closer to an understanding of the true description of the gap length as compared to the prior distribution. Mathematically, then, the goal here is to obtain the sensor-design $e^* \in \Omega_E$ that yields the maximum relative gain in the information contained in the $f_{\Theta|X_e}(\theta|x_e)relativetotheinformationcontainedin\color{black}{f}_{\rTheta}\left(\theta \right)$.

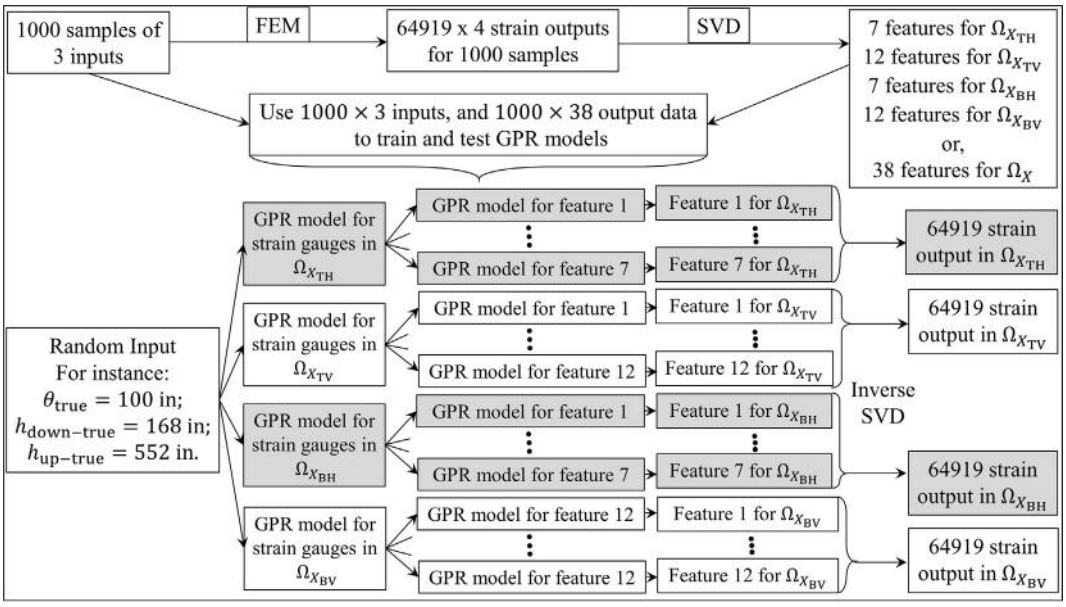

Fig. 4. Flowchart describing strain data generation using FEM, and prediction using GPR surrogate model.

We very briefly describe the remaining three steps of optimization next. The details are omitted in this brief description because each of these steps demands a complete section on its own.

2.3.2. Step 2: Definition of the design dependent Bayes risk functional

The next step of the Bayesian optimization is to define the optimality criterion or the objective functional, which is otherwise known as Bayes risk. The Bayes risk is a function of the design $e \in \Omega_E$ and is denoted by $\mathfrak{E}(e)$. Bayes risk is a problem-dependent functional. We aim to define Bayes risk such that:

1. The Bayes risk guides us to obtain a sensor-design that maximizes information gains on the gap length inferred from the sensor measurements. The gain in the information is quantified by the *f*-divergence that evaluates the similarity between two probability measures.
2. The Bayes risk incorporates the desire to obtain better information/description of the gap length when the structure approaches a higher degree of damage (an increased gap length approaching some critical size). This is accomplished by using a risk-based weight function.
3. The Bayes risk also takes into account prior knowledge of the gap length.

The Bayes risk for this paper is defined as the integral of the weighted *f*-divergence of the posterior distribution relative to the prior distribution, weighted over the prior distribution, and risk-based weight function, integrated over all the physically possible values of the gap length. Section 3 is dedicated to detailing the Bayes risk functional.

2.3.3. Step 3: Evaluation of the design-dependent Bayes risk functional

Bayes risk is a non-linear functional. For a given design *e*, evaluating the Bayes risk requires one to obtain the posterior of the gap length and risk-based weight functions. Section 3.2 delineated a line of reasoning for incorporating risk-based weight function in the definition of the Bayes risk. Theoretically, the posterior distribution can be evaluated using Bayes' theorem:

$$f_{\Theta|X_e}(\theta|\boldsymbol{x}_e) = \frac{f_{X_e|\Theta}(\boldsymbol{x}_e|\theta) f_{\Theta}(\theta)}{f_{X_e}(\boldsymbol{x}_e)}. \tag{6}$$

The quantity $f_{\Theta}(\theta)$ represents the prior probability of the true state, and in absence of any information, it may be assumed to be a uniform (uninformed) distribution. The likelihood $f_{X_e|\Theta}(x_e|\theta)$ is obtained using either a physics-based model or a digital twin. We note that the posterior does not follow a canonical distribution and expectations with respect to the posterior in (6) cannot be obtained analytically. This is because the relationship between strain measurements x_e and the gap length θ is highly nonlinear. We deploy numerical approximation of the posterior distribution by using particle filters, or specifically a sequential Monte Carlo (SMC) approach.

The integrand in the Bayes risk expression is integrated over the gap length (defined later in Section 3). The second difficulty in obtaining Bayes risk is to evaluate this integral. To approximate the integral, we first change the variable of the integral from the measurement space to the uncertain input space. For instance, in our problem, the hydrostatic heads and the noise in the strain values are the primary random input variables. Since there is a unique one-to-one relationship between an input realization and an output realization, this allows us to change the variables of integration in the Bayes risk. The integral can then be numerically approximated using univariate dimensional reduction and Gauss-Hermite quadrature. Section 4 discusses the approach to evaluate the Bayes risk.

2.3.4. Step 4: Obtaining the optimal sensor design using Bayesian optimization

With the problem well-defined (step 1) and the associated Bayes risk optimality criterion formulated (steps 2–3), the problem becomes: "Given $\Omega_\Theta, \Omega_{X_e}, \Omega_E, \Omega_\zeta, \Omega_{h_{\text{up}}}, \Omega_{h_{\text{down}}}$, given an assumed uncertainty structure (as in Eq. (4) and (5)), what is the design $e^* \in \Omega_E$ that maximizes the Bayes risk objective functional $\mathfrak{E}(e)$?" We carefully note that intuitively, "*risk*" must be minimized. However, in this paper, *Bayes risk* represents relative gain in information, and therefore, must be maximized. We could have called the objective function "*Bayes utility*", but as noted in the introduction, we take advantage of the fact that "*risk*" is a subjective quantity.

We very briefly detail the sensor optimization algorithm, which will be explained in great depth in Section 5. We start with an initial design e_0 consisting of N_0 number of sensors. To obtain the optimal design e_1 with (N_0+1) sensors, we search the entire design space for the $(N_0+1)^{\text{th}}$ sensor location. The $(N_0+1)^{\text{th}}$ sensor location that maximizes the acquisition function constitutes the next additional sensor. In this paper, we use *expected improvement* [50,51] as the acquisition function. Similarly, we repeat the optimization process to arrive at the optimal design $e_{n_{\text{as}}}$ consisting of $N_0 + n_{\text{as}}$ sensors (or n_{as} number of additional sensors relatively to the initially assumed design e_0). Finally, we pick $e^* = \text{argmax}_{e_{n_{\text{as}}}} \mathfrak{E}(e_{n_{\text{as}}})$ as the most optimal design, where $\mathfrak{E}(e_{n_{\text{as}}})$ represents the Bayes risk associated with the design $e_{n_{\text{as}}}$. Section 5 details the Bayesian optimization algorithm for optimal sensor placement.

2.4. Bayesian inference of gap length for a given sensor design

As discussed in the previous section, the state parameter is the gap length θ, and for a given sensor-design e, the measurement vector $x_e \in \Omega_{X_e}$ is the strain recorded at $N_{sg}(e)$ number of strain gauge locations. Therefore, X_e is also a random vector. The measurements obtained from the strain gauges are used to infer the gap length θ using Eq. (6). In the context of inferring θ, the evidence $f_{X_e}(x_e)$ is just a normalizing constant. Therefore, Eq. (6) may be written as:

$$f_{\Theta|X_e}(\theta|x_e) \propto f_{X_e|\Theta}(x_e|\theta) f_\Theta(\theta). \tag{7}$$

The distribution $f_\Theta(\theta)$ reflects the prior knowledge about the parameter θ before any new information/measurements are obtained. Assuming only basic geometrical constraints on the gap length, we assume the prior to be a uniform distribution spanning over $\Omega_\Theta = [\theta_{\text{low}}, \theta_{\text{up}}]$, such that

$$f_\Theta(\theta) = \begin{cases} (\theta_{\text{up}} - \theta_{\text{low}})^{-1}, & \theta \in \Omega_\Theta; \\ 0, & \text{otherwise}. \end{cases} \tag{8}$$

Evaluating the posterior using Eq. (7) requires us to obtain the likelihood $f_{X_e|\Theta}(x_e|\theta)$. Constructing the likelihood $f_{X_e|\Theta}(x_e|\theta)$ requires a model of the measurement process. We note that the design e consists of the selected sensors chosen from a total of 64919×4 possibilities, or $\Omega_{X_e} \subset \Omega_X$. For a given gap length and the hydrostatic heads, the FEM or GPR yields strain values for all of the 64919×4 sensors. Therefore, to detail the measurement model, we consider the total measurement space Ω_X. In this paper, we use the following measurement model

$$x = g(\theta, h_{\text{up}}, h_{\text{down}}) + \varepsilon. \tag{9}$$

In the equation above, $x = (x_1, x_2, \cdots, x_{64919\times4}) \in \Omega_X$ is a realization of the random vector X consisting of 64919×4 strain measurements, where x_i represents the strain value corresponding to the i^{th} strain gauge. For a given gap length θ, the digital surrogate g yields $g(\theta, h_{\text{up}}, h_{\text{down}}) = (g_1(\theta, h_{\text{up}}, h_{\text{down}}), g_2(\theta, h_{\text{up}}, g_{\text{down}}), \cdots, g_{64919\times4}(\theta, h_{\text{up}}, h_{\text{down}}))$ at 64919×4 location of the strain gauges, where $g_i(\theta, h_{\text{up}}, h_{\text{down}})$ represents the strain response of the i^{th} strain gauge obtained by the GPR surrogate model g. In the equation above $\varepsilon \in \Omega_\zeta$ is the realization of the random vector ζ defining the noise in 64919×4 sensors.

Eq. (9) defines the measurement model considering all the sensor locations in Ω_X. However, a design e consists of only $N_{sg}(e)$ sensors with the measurement space Ω_{X_e}. Utilizing the fact that $\Omega_{X_e} \subset \Omega_X$, let g_e define the *true* strain response for the sensors included in design e obtained by the GPR model, such that $g_e(\theta, h_{\text{up}}, h_{\text{down}}) = \left(g_{e_1}(\theta, h_{\text{up}}, h_{\text{down}}), \cdots, g_{e_{N_{sg}(e)}}(\theta, h_{\text{up}}, h_{\text{down}})\right)$. Similarly, let $x_e = \left(x_{e_1}, \cdots, x_{e_{N_{sg}(e)}}\right) \in \Omega_{X_e}$ denotes the *observed/measured* strain response. Here, $g_{e_i}(\theta, h_{\text{up}}, h_{\text{down}})$ and x_{e_i} represents the *true* (obtained by the GPR model) and the *observed* strain response of the i^{th} strain gauge in the sensor design e, respectively. The measurement model for the strain gauges included in the design e is given by

$$x_e = g_e(\theta, h_{\text{up}}, h_{\text{down}}) + \varepsilon_e. \tag{10}$$

In the equation above, x_e is one of the realizations of the random vector X_e. The vector ε_e is the realization of the random vector ζ_e with $\varepsilon_e = (\varepsilon_1, \varepsilon_2, \cdots, \varepsilon_{N_{sg}(e)})$. It represents the measurement noise/error vector for the design e, where ε_i denotes the error between the measurement output and GPR predicted response (assumed to be the true response) corresponding to the i^{th} strain gauge in the design e as defined in Eq. (5). We assume that ε_e follows a zero-mean Gaussian distribution with independent components, i.e., the noise/error terms of all $N_{sg}(e)$ strain gauges are assumed to be statistically independent. In addition, we assume that each strain gauge has same standard-deviation σ_{ε_i}, such that

$$f_{\zeta_e}(\varepsilon_e = (\varepsilon_1, \cdots, \varepsilon_{N_{sg}(e)})) = \prod_{i=1}^{N_{sg}(e)} f_{\zeta_i}(\varepsilon_i) = \prod_{i=1}^{N_{sg}(e)} \frac{1}{\sigma_{\varepsilon_i}} \phi\left(\frac{\varepsilon_i}{\sigma_{\varepsilon_i}}\right). \tag{11}$$

Using the measurement model defined in Eq. (10), and the description of noise in Eq. (11), the likelihood of observing the strain measurement $x_e \in \Omega_{X_e}$ for the gap length θ can be written as

$$f_{X_e|\Theta}(x_e|\theta) = \prod_{i=1}^{N_{sg}(e)} \frac{1}{\sigma_{\varepsilon_i}} \phi\left(\frac{x_{e_i} - g_{e_i}(\theta, h_{\text{up}}, h_{\text{down}})}{\sigma_{\varepsilon_i}}\right). \tag{12}$$

Having defined the prior and the likelihood in Eq. (8) and (12), we note that the posterior cannot be obtained analytically using Eq. (6). This is because the relationship between strain measurements x_e and the gap length θ is highly nonlinear. One can rely on numerical approximation techniques like Markov chain Monte Carlo (MCMC) methods, particle filter, and sequential Monte Carlo (SMC) approach in recursive mode to solve the inference problem. As mentioned, because the evaluation of the likelihood $f_{X_e|\Theta}(x_e|\theta)$ at numerous values of θ using the full finite element model was too expensive, this was achieved by running instead the the GPR model g_e. Furthermore, we employ the particle filter method (or sequential Monte Carlo (SMC) in recursive mode) to obtain the posterior.

We also simulate the measurement data numerically. For simulating such data, we obtain the response of the digital surrogate $g(\theta_{\text{true}}, h_{\text{up-true}}, h_{\text{down-true}})$ parameterized by a chosen/fixed value of true gap length θ_{true} subjected to chosen/fixed input loading $(h_{\text{up-true}}, h_{\text{down-true}})$. This strain gauge response is now corrupted by Gaussian noise of standard deviation σ_{ε_i} to mimic the real-world measurement noise. This corrupted strain response is now used as the measurement/observed data $x_e \in \Omega_{X_e}$.

Obtaining the posterior numerically using particle filtering requires evaluating the likelihood at numerous values of the gap length, called the particles. Usually, particle filtering is used for sequential updating of the posterior distribution for a dynamic system, i.e., the case where new information on the system is available as time evolves. However, in this case, we just have one set of data, and we aim at obtaining the posterior in a single step. The following summarizes the process of obtaining the posterior distribution of the gap length:

(a)For the assumed true gap length θ_{true} and the chosen/fixed input loading $(h_{\text{up-true}}, h_{\text{down-true}})$, simulate the observed/measurement strain data $x_e \in \Omega_{X_e}$.
(b)We choose $N_{\text{particle}} = 5000$ discrete values of the gap length, called particles. It is at these 5000 particles for the likelihood is to be evaluated.
(c)At each of these 5000 particles (or the gap length), and for a given loads $(h_{\text{up-true}}, h_{\text{down-true}})$, the GPR model yields the *true* strain value at the i^{th} strain location for the gap length particle θ_j is denoted by $g_{e_i}(\theta_j, h_{\text{up-true}}, h_{\text{down-true}})$, where $i \leqslant N_{\text{sg}}(e)$ and $j \leq 5000$. We obtain the numerical value of the likelihood of the measurement given the gap length θ_j at the observed strain $x_e \in \Omega_{X_e}$ using Eq. (12) as:

$$f_{X_e|\Theta}(x_e|\theta_j) = \prod_{i=1}^{N_{\text{sg}}(e)} \frac{1}{\sigma_{\varepsilon_i}} \phi\left(\frac{x_{e_i} - g_{e_i}(\theta_j, h_{\text{up}}, h_{\text{down}})}{\sigma_{\varepsilon_i}}\right). \tag{13}$$

In the equation above, x_{e_i} represents the observed strain value at the i^{th} strain gauge.
(d)Evaluate the weight w_j for each particle as:

$$w_j = \frac{f_{X_e|\Theta}(x_e|\theta_j)}{\sum_{k=1}^{N_{\text{particle}}} f_{X_e|\Theta}(x_e|\theta_k)}. \tag{14}$$

(e)Calculate the cumulative weights to observe big jumps. Resample the weighted particles to obtain unweighted samples of the posterior distribution over gap length.

It is evident from discussion carried above that evaluating the posterior distribution of the gap length θ for a given sensor measurements X_e requires obtaining the likelihood $f_{X_e|\Theta}(x_e|\theta_j)$ for $j \leqslant N_{\text{particles}}$. This requires running the GPR model $N_{\text{particles}}$ times.

3. The objective functional, Bayes risk

3.1. Bayes risk: Expected utility function

Recall Step 2 of the Bayesian optimization framework discussed in Section 2.3. There are three primary goals that we aim to achieve: (1) Maximize the relative gain in the information; (2) Obtain better information/description of the gap length when the true value of gap length is larger or the state of the structure approaches a higher degree of damage; (3) Include the prior knowledge of the gap length.

3.1.1. Relative gain of information: f-divergence

We start with the first goal. As discussed before, the prior distribution of gap length $f_\Theta(\theta)$ quantifies our understanding of the gap length when no additional/new information on the system (through the strain gauge measurements) is available. When the new information or the sensor measurements $x_e \in \Omega_{X_e}$ are available, Bayesian inference allows us to refine our understanding of the gap length, now quantified by the posterior $f_{\Theta|X_e}(\theta|x_e)$. In this section, for brevity, we denote the posterior distribution as $f_{\Theta|X_e}(\theta|x_e) = g_\Theta(\theta)$. Traditionally, the *information divergence* (similarity or dissimilarity) between two distributions, for example, deviation of the posterior $g_\Theta(\theta)$ from the prior $f_\Theta(\theta)$, is quantified by the relative entropy or Kullback–Leibler (KL) divergence or i-divergence (i for information), defined by:

$$D_{KL}(g_\Theta(\theta)||f_\Theta(\theta)) = \int_{\Omega_\Theta} g_\Theta(\theta) \log\left(\frac{g_\Theta(\theta)}{f_\Theta(\theta)}\right) \mathrm{d}\theta. \tag{15}$$

Since KL divergence is not symmetric, we prefer this form of information divergence because it quantifies the information gain in the posterior distribution of the gap length as compared to the prior distribution (refer to [52,53]). Although KL

divergence measures the distance between two probability distributions, it does not qualify as a statistical *metric* of spread because it violates the symmetric property and triangular inequality. However, KL divergence does satisfy the other two properties of a metric: non-negativity and the identity of indiscernible. Therefore, KL divergence of probability distributions may be loosely interpreted as a *nonsymmetric* analog of squared Euclidean distance. Like KL divergence, there are many other divergences used to evaluate the similarity and dissimilarity between probability distributions. Many of these divergences can be unified under the generic framework of *f*-divergence [54]. Therefore, i-divergence is a special case of *f*-divergence. For a convex function $\mathscr{f}(t)$ defined for $t > 0$, with $\mathscr{f}(1) = 0$, the *f*-divergence of the posterior $g_\Theta(\theta)$ from the prior $f_\Theta(\theta)$ is defined by:

$$D_{\mathscr{f}}(g_\Theta(\theta)||f_\Theta(\theta)) = \int_{\Omega_\Theta} f_\Theta(\theta)\mathscr{f}\left(\frac{g_\Theta(\theta)}{f_\Theta(\theta)}\right)\mathrm{d}\theta. \tag{16}$$

Note that the constraint $\mathscr{f}(1) = 0$ implies that all the *f*-divergences satisfy the identity of indiscernible. Table 1 in Appendix A lists some of the important and commonly used *f*-divergences; more information may be found in [54–57]. Among all the *f*-divergences listed in Table 1 (see Appendix A), only the total variance satisfies all the properties of a metric: non-negativity, symmetry, the identity of indiscernible, and triangular inequality [58].

In this paper, the state parameter (the gap length) is a single-dimensional quantity. However, in many problems, the state parameter is a multi-dimensional vector. In such scenarios, evaluating the *f*-divergence becomes computationally expensive. Many approximation techniques for *f*-divergence have been proposed, like using higher-order Chi distances [56], penalized convex risk minimization [59], and random mixture estimator [60]. For completion's sake and for ensuring generality, we briefly present approximating *f*-divergence using Taylor series expansion and higher-order Chi distances [56]. The function $\mathscr{f}(t)$ can be expanded about the point t_0 using the Taylor series as

$$\mathscr{f}(t) = \sum_{i=0}^{\infty} \frac{1}{i!}(t - t_0)^i . \frac{\partial^i \mathscr{f}(t)}{\partial t^i}|_{t=t_0}. \tag{17}$$

The *f*-divergence defined in Eq. (16) can be written as:

$$\begin{aligned} D_{\mathscr{f}}(g_\Theta(\theta)||f_\Theta(\theta)) &= \int_{\Omega_\Theta} f_\Theta(\theta)\sum_{i=0}^{\infty}\frac{1}{i!}\left(\frac{g_\Theta(\theta)}{f_\Theta(\theta)} - t_0\right)^i . \frac{\partial^i \mathscr{f}(t)}{\partial t^i}|_{t=t_0}\mathrm{d}\theta = \sum_{i=0}^{\infty}\frac{1}{i!}\frac{\partial^i \mathscr{f}(t)}{\partial t^i}|_{t=t_0}\left(\int_{\Omega_\Theta}\frac{(g_\Theta(\theta) - t_0 f_\Theta(\theta))^i}{f_\Theta(\theta)^{i-1}}\mathrm{d}\theta\right) \\ &= \sum_{i=0}^{\infty}\frac{1}{i!}\frac{\partial^i \mathscr{f}(t)}{\partial t^i}|_{t=t_0} . D_{\chi^i_{P,t_0}}(g_\Theta(\theta)||f_\Theta(\theta)). \end{aligned} \tag{18}$$

Here, $D_{\chi^i_{P,t_0}}(g_\Theta(\theta)||f_\Theta(\theta))$ is the generalization of the i^{th} order Pearson-Vajda *f*-divergence. The equation above allows us to write any *f*-divergence as the weighted sum of the generalized i^{th} order Pearson-Vajda *f*-divergence, which in turn can be approximated by the restricted class of exponential families that are easy to evaluate [56].

Table 1
Common *f*-divergences.

Types of *f*-divergences	Denoted by	Function $\mathscr{f}(t)$
Kullback–Leibler	$D_{KL}(g_\Theta(\theta)\|\|f_\Theta(\theta))$	$t\log t$
Reverse Kullback–Leibler	$D_{KL}(f_\Theta(\theta)\|\|g_\Theta(\theta))$	$-\log t$
Pearson Chi Square	$D_{\chi^2_P}(g_\Theta(\theta)\|\|f_\Theta(\theta))$	$(t-1)^2$
Neyman Chi Square	$D_{\chi^2_N}(g_\Theta(\theta)\|\|f_\Theta(\theta))$	$\frac{(1-t)^2}{t}$
Pearson-Vajda	$D_{\chi^k_P}(g_\Theta(\theta)\|\|f_\Theta(\theta))$	$(t-1)^k$
Squared Hellinger	$D_{H^2}(g_\Theta(\theta)\|\|f_\Theta(\theta))$	$\left(\sqrt{t}-1\right)^2$
Total variation	$D_\delta(g_\Theta(\theta)\|\|f_\Theta(\theta))$	$\frac{1}{2}\|t-1\|$
K-divergence	$D_K(g_\Theta(\theta)\|\|f_\Theta(\theta))$	$t\log\left(\frac{2t}{t+1}\right)$
Skewed *K*-divergence	$D_{K_\alpha}(g_\Theta(\theta)\|\|f_\Theta(\theta))$	$t\log\left(\frac{t}{1+\alpha(1-t)}\right)$
Jensen-Shannon	$D_{JS}(g_\Theta(\theta)\|\|f_\Theta(\theta))$	$\frac{1}{2}\left(t\log t - (t+1)\log\left(\frac{t+1}{2}\right)\right)$
α Jensen-Shannon	$D_{JS_\alpha}(g_\Theta(\theta)\|\|f_\Theta(\theta))$	$\frac{1}{2}\left(t\log t - (t+1)\log(1+\alpha(t-1))\right)$
α-divergence	$D_\alpha(g_\Theta(\theta)\|\|f_\Theta(\theta))$	$\begin{cases}\frac{4}{1-\alpha^2}\left(1-t^{\frac{1+\alpha}{2}}\right) & \alpha \neq \pm 1;\\ t\log t & \alpha = 1;\\ -\log t & \alpha = -1.\end{cases}$
$\mathscr{f}_\beta$-divergence	$D_{\mathscr{f}_\beta}(g_\Theta(\theta)\|\|f_\Theta(\theta))$	$\begin{cases}\frac{\beta}{\beta-1}\left(\left(1+t^\beta\right)^{\frac{1}{\beta}} - 2^{\left(\frac{1}{\beta}-1\right)}(1+t)\right) & \beta \in \mathbb{R}n\{1\};\\ t\log t - (1+t)\log\frac{1+t}{2} & \beta = 1;\\ \frac{1}{2}\|t-1\| & \beta = \infty.\end{cases}$

3.1.2. Implicit and explicit inclusion of the risk weights into Bayes risk

The space of all the uncertainties in the current problem is defined as $\Omega_{\xi_e} = \Omega_{H_{\text{up}}} \times \Omega_{H_{\text{down}}} \times \Omega_{\zeta_1} \times \Omega_{\zeta_2} \times \cdots \times \Omega_{\zeta_{N_{\text{sg}}(e)}}$, such that the random variable ξ_e represents all the uncertainty sources considered to affect the design e. Let $\beta_e = \left(h_{\text{up}}, h_{\text{down}}, \varepsilon_1, \varepsilon_2, \cdots, \varepsilon_{N_{\text{sg}}(e)}\right) \in \Omega_{\xi_e}$ represents a realization of the random variable ξ_e. Secondly, since the strain measurements $x_e \in \Omega_{X_e}$ are representative of the physics of the miter gate, its value also depends on the gap length value $\theta \in \Omega_\Theta$. This fact is mathematically denoted by redefining the random variable X_e to be a function of the uncertainties and the true gap length, $x_e = X_e(\theta_{\text{true}}, \beta_e)$. If there is no external noise and if the true value of gap length θ_{true} exactly known, then x_e represents true value of the strain measurements. However, since the true gap length can't be obtained under all the inevitable uncertainty, the best one can do is to define the Bayes risk as the expected value of risk-weighted f-divergence averaged over the entire space Ω_Θ and Ω_{ξ_e}, i.e., by considering the entire range of possible true values of the gap length and taking into account the uncertainties in strain gauge readings and external loads. We reasonably assume that the random variables $\Theta, H_{\text{up}}, H_{\text{down}}$, and ζ_i are statistically independent. With all the necessary pieces defined, we first state the Bayes risk functional without including any risk weights as

$$\mathfrak{E}(e) = \int_{\Omega_\Theta} \int_{\Omega_{\xi_e}} f_{\xi_e}(\beta_e) f_\Theta(\theta) D_f\left(f_{\Theta|X_e(\theta_{\text{true}}=\theta,\beta_e)}(\varphi|x_e)||f_\Theta(\varphi)\right) \mathrm{d}\beta_e \mathrm{d}\theta. \tag{19}$$

In the equation above, the variable φ gets integrated out in the expression of f-divergence. The f-divergence is a function of $(\theta_{\text{true}} = \theta, \beta_e)$, in the sense that

$$D_f\left(f_{\Theta|X_e(\theta_{\text{true}}=\theta,\beta_e)}(\varphi|x_e)||f_\Theta(\varphi)\right) = \int_{\Omega_\Theta} f_\Theta(\varphi) f\left(\frac{f_{\Theta|X_e(\theta_{\text{true}}=\theta,\beta_e)}(\varphi|x_e)}{f_\Theta(\varphi)}\right) \mathrm{d}\varphi = \mathscr{D}_f(\theta_{\text{true}} = \theta, \beta_e). \tag{20}$$

In the Eq. (19) and (20), the f-divergence $\mathscr{D}_f(\theta_{\text{true}} = \theta, \beta_e)$ measures the divergence in the posterior distribution in the gap length relative to its prior distribution.

We consider two approaches to incorporate the risk weights in the Bayes risk. In the first approach, we *explicitly weigh* the integrand of the Bayes risk defined in Eq. (19) with the risk weights, such that

$$\mathfrak{E}_{\text{explicit-risk}}(e) = \int_{\Omega_\Theta} \int_{\Omega_{\xi_e}} f_{\xi_e}(\beta_e) f_\Theta(\theta) \mathrm{r}(\theta_{\text{true}} = \theta) \mathscr{D}_f(\theta_{\text{true}} = \theta, \beta_e) \mathrm{d}\beta_e \mathrm{d}\theta. \tag{21}$$

The quantity $\mathrm{r}(\theta_{\text{true}} = \theta)$ weighs the risk-based importance factor for all the possible value of true gap length, i.e. $\forall\, \theta_{\text{true}} = \theta \in \Omega_\Theta$. The prior $f_\Theta(\theta)$ accounts for the prior knowledge of the gap length, and the distribution $f_{\xi_e}(\beta_e)$ accounts for all the uncertainties. Finally, we define the utility function $\mathscr{L}(\theta_{\text{true}} = \theta, \beta_e)$ as the risk-weighted f-divergence

$$\mathscr{L}(\theta_{\text{true}} = \theta, \beta_e) = \mathrm{r}(\theta_{\text{true}} = \theta) \mathscr{D}_f(\theta_{\text{true}} = \theta, \beta_e). \tag{22}$$

We understand that in the definition of the Bayes risk,*we consider all the possible values of the true gap length*. From here on, we omit writing $\theta_{\text{true}} = \theta$ in the argument of utility or the weight function, such that Eq. (22) becomes

$$\mathscr{L}(\theta, \beta_e) = \mathrm{r}(\theta) \mathscr{D}_f(\theta, \beta_e). \tag{23}$$

In the equation above, the argument θ represents *one possibility of true gap length*.

With the simplified notation of f-divergence and definition of the utility function, $\mathscr{L}(\theta, \beta_e)$, and the Bayes risk explicitly considering the risk weights is compactly written as

$$\mathfrak{E}_{\text{explicit-risk}}(e) = E_{\Theta\xi_e}[\mathscr{L}(\theta, \beta)] = \int_{\Omega_\Theta} \int_{\Omega_{\xi_e}} f_\Theta(\theta) f_{\xi_e}(\beta_e) \mathrm{r}(\theta) \mathscr{D}_f(\theta, \beta_e) \mathrm{d}\beta_e \mathrm{d}\theta. \tag{24}$$

Another mathematically equivalent approach to consider risk weighing is by modifying the prior distribution to

$$f_{\hat{\Theta}}\left(\hat{\theta} = \theta\right) = \frac{f_\Theta(\theta) \mathrm{r}(\theta)}{\int_{\theta_{\text{low}}}^{\theta_{\text{up}}} f_\Theta(\theta) \mathrm{r}(\theta) \mathrm{d}\theta}, \tag{25}$$

such that $f_{\hat{\Theta}}\left(\hat{\theta}\right)$ is *transformed prior probability* distribution function of the random variable $\Theta \longrightarrow \hat{\Theta}$ with the realization $\hat{\theta} \in \Omega_{\hat{\Theta}}$, such that $\Omega_\Theta = \Omega_{\hat{\Theta}}$. The Bayes risk that *implicitly* incorporates the risk weight in the form of modified prior distribution is defined as

$$\mathfrak{E}_{\text{implicit-risk}}(e) = E_{\hat{\Theta}\xi_e}\left[\mathscr{D}_f\left(\hat{\theta}, \beta_e\right)\right] = \int_{\Omega_\Theta} \int_{\Omega_{\xi_e}} f_{\hat{\Theta}}\left(\hat{\theta}\right) f_{\xi_e}(\beta_e) \mathscr{D}_f\left(\hat{\theta}, \beta_e\right) \mathrm{d}\beta_e \mathrm{d}\hat{\theta}. \tag{26}$$

The Bayes risk functional $\mathfrak{E}_{\text{implicit-risk}}(e)$ *implicitly* considers the risk-weight $r(\theta)$. We note that the implicit Bayes risk $\mathfrak{E}_{\text{implicit-risk}}(e)$ and the explicit Bayes risk $\mathfrak{E}_{\text{explicit-risk}}(e)$ are proportional to each other, with a positive constant of proportionality, i.e., $\left(\int_{\theta_{\text{low}}}^{\theta_{\text{up}}} f_\Theta(\theta) \mathrm{r}(\theta) \mathrm{d}\theta\right)$:

$$\mathfrak{E}_{\text{implicit-risk}}(e) \propto \mathfrak{E}_{\text{explicit-risk}}(e). \tag{27}$$

Therefore, either explicit or implicit Bayes risk can be used in the optimization problem. Finally, we note that the implicit and explicit Bayes risk converge when we assign a constant risk-weight (importance factor) to all the true gap length values, such that

$$\mathfrak{E}(e) = \mathfrak{E}_{\text{implicit-risk}}(e)|_{r(\theta)=1} = \mathfrak{E}_{\text{explicit-risk}}(e)|_{r(\theta)=1}. \tag{28}$$

As shown in Eq. (24) Bayes risk is defined as the expected value of the utility function. Ideally, the goal is to maximize the utility, but due to the uncertainties in the system quantified by $\beta_e \in \Omega_{\zeta_e}$, and our inability to know the true value of the gap length, the best we can do is to pick a sensor design that maximizes the expected value of the utility averaged over all the possible values of the true gap length and the uncertainties. An optimal sensor design that maximizes the expected utility is the most optimal. The next Section 3.2 discusses the quantity $r(\theta_{\text{true}})$ in detail.

Evaluating the f-divergence $\mathscr{D}_f(\theta, \beta_e)$ for a given true gap length $\theta_{\text{true}} = \theta$ and the external uncertainties β_e (consisting of hydrostatic heads and the noise in strain gauge readings) requires us to obtain the posterior distribution $f_{\Theta|X_e(\theta,\beta_e)}(\varphi|x_e)$ of the gap length for a given true-variables (θ, β_e). Therefore, as was mentioned above, for a given measurement $X_e(\theta, \beta_e)$, obtaining the posterior using particle filter requires running the GPR or digital surrogate model $N_{\text{particles}}$ times. However, since we are simulating the measurement data $X_e(\theta, \beta_e)$, we need to run GPR model once as mentioned in Eq. (10). Therefore, evaluating the f-divergence $\mathscr{D}_f(\theta, \beta_e)$ (or the utility $\mathscr{L}(\theta, \beta_e)$) requires running the GPR model $(N_{\text{particles}} + 1)$ times.

For the prior $f_\Theta(\varphi)$ and the posterior distribution $f_{\Theta|X_e(\theta,\beta_e)}(\varphi|x_e)$, the f-divergence is numerically evaluated by approximating Eq. (20) as:

$$\mathscr{D}_f(\theta, \beta_e) \approx \frac{1}{N}\sum_{i=1}^{N} r(\varphi_i) \mathscr{f}\left(\frac{f_{\Theta|X_e(\theta,\beta_e)}(\varphi_i|x_e)}{f_\Theta(\varphi_i)}\right). \tag{29}$$

Fig. 5 illustrates a function or a module called "*Evaluate the Utility* $\mathscr{L}(\theta, \beta_e)$" or "*Evaluating the f-divergence* $\mathscr{D}_f(\theta, \beta_e)$" that obtains the f-divergence $\mathscr{D}_f(\theta, \beta_e)$ and the utility $\mathscr{L}(\theta, \beta_e)$ for a given design e and the input variables (θ, β_e). Note that obtaining utility function is just a step away from the f-divergence. It does so in a three step process that requires running the GPR model $(N_{\text{particles}} + 1)$ times. The first step is to simulate observed/measurement data x_e for a design e by assuming a true gap length θ, hydraulic heads $(h_{\text{up}}, h_{\text{down}})$, and a noise structure $f_{\zeta_i}(\varepsilon_i)$. The second step is to obtain the posterior distribution of the gap length given the measurement x_e obtained in the first step using particle filter. Finally, the third step is to evaluate f-divergence of the posterior (obtained in step 2) relative to the prior distribution of the gap length that ultimately yields the utility function.

3.2. Risk-based weight function

In some applications, there is a well-defined limit state that defines damage criticality, and a given structural owner/stakeholder might want an SHM system to determine the proximity to that limit state. In the current application, there is no well-defined limit state, and the risk weight function $r(\theta_{\text{true}})$ can serve as a surrogate to that proximity by assigning relative importance to the values of true gap length θ_{true} in terms of the degree of damage. For instance, $r(\theta_{\text{true}} = \theta_2) > r(\theta_{\text{true}} = \theta_1)$ implies that the structural owner believes a gap length of θ_2 is more concerning with regard to criticality than when the true gap length is θ_1. This approach is inspired by the fact that different decision-makers mentally assign a different importance factor (or in economic terms: utility or risk-intensity) to the seriousness/urgency to take necessary actions with the increasing intensity of structural damage. For instance, given that the true state of the structure is moderately damaged, a decision-maker who is fearful of making any mistake leading to heavy losses, a *risk-averter*, might suggest major repair and continuous inspection. On the other hand, another decision-maker might suggest only minor repairs, a *risk-seeker*. Commensurate with the notion of subjective risk perception, we suggest risk weights $r(\theta_{\text{true}})$ that follow the following two properties:

1. The risk weights $r(\theta_{\text{true}})$ must have a zero or positive slope. This is because, physically, an increase in gap length reflects higher damage to the structural state of the miter gate. Therefore, to satisfy this physical constraint, we can either assign constant or monotonically increasing risk weights for all the gap lengths.
2. The risk weight need not be unique and can be selected based on a desirable optimization criterion. For example, if we decide to equally weigh all the values of true gap length, then the risk weight can be taken as a constant $r(\theta_{\text{true}}) = 1$ (zero slope). On the other hand, if we desire to make a better prediction of the state of the miter gate at a higher gap length value that implies higher damage, we may pick a monotonically increasing risk weight.Since the state estimation depends on the probabilistic description of the gap length, obtaining a better estimate of the miter gate damage intensity demands a better estimate of the probability distribution of the gap length. We aim at assigning an increasing importance factor to damage estimation as the value of the gap length increases. Therefore, for the sake of the optimization problem considered in this paper, we consider a particular case of monotonically increasing risk-weight of the following form:

$$r(\theta_{\text{true}}) = e^{-\left(\frac{\theta_{\text{true}} - \theta_{\text{critical}}}{b}\right)^2}, \text{for } \theta_{\text{low}} < \theta_{\text{true}} < \theta_{\text{up}} = \theta_{\text{critical}}. \tag{30}$$

In the equation above, θ_{critical} represents the critical value of gap length such that as the true gap length θ_{true} approaches this critical value θ_{critical}, the risk-weight increases. We consider $\theta_{\text{critical}} = \theta_{\text{up}}$. The factor b controls how quickly the risk-weight

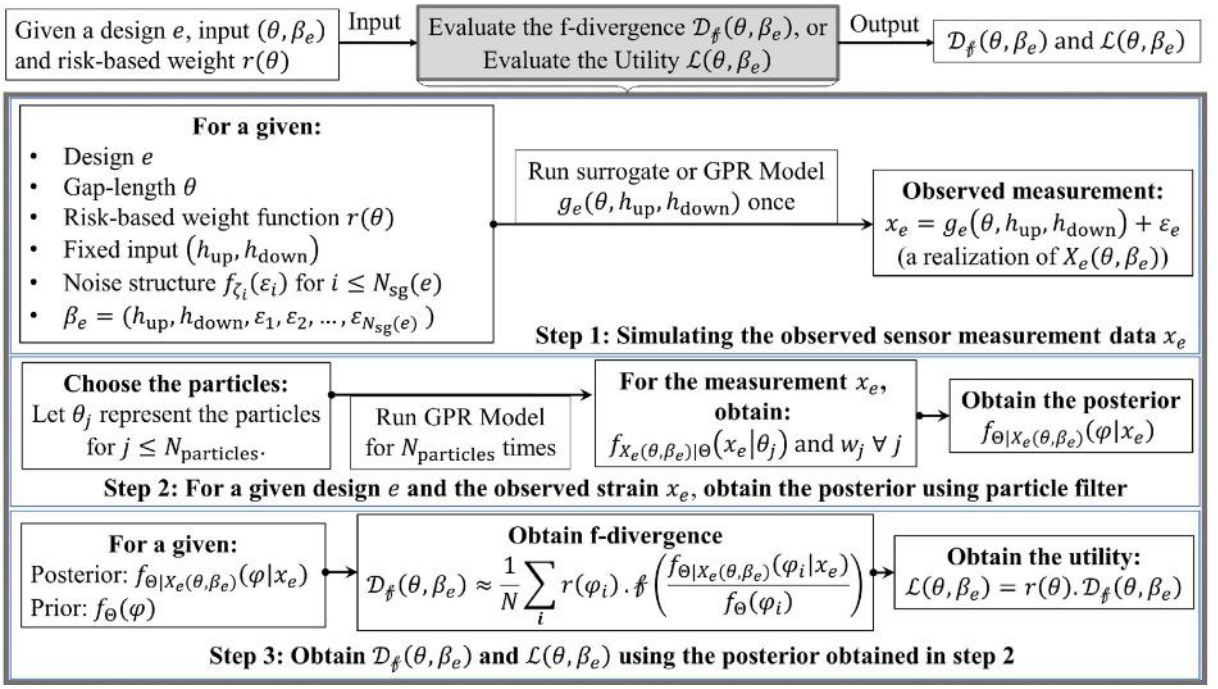

Fig. 5. Evaluating the *f*-divergence $\mathscr{D}_f(\theta, \beta_e)$ and the utility $\mathscr{L}(\theta, \beta_e)$ for a given case of true gap length θ, uncertainties β_e, and the risk-based weight function $r(\theta)$.

decays as θ_{true} deviates from θ_{critical}. Now with the Bayes risk functional fully defined, the next section deals with evaluating the Bayes risk.

4. Evaluating the Bayes risk for a fixed sensor design

4.1. Revisiting Bayes risk

Section 3.1 defined the utility function $\mathscr{L}(\theta, \beta_e)$, and the explicit Bayes risk was defined as the expected utility, i.e., averaged over all the values of the uncertainties $\beta_e \in \Omega_{\xi_e}$, and the possible true values of gap length $\theta \in \Omega_\Theta$. We note that these random variables constituting β_e and θ (or $\hat{\theta}$ when Bayes risk considers the risk-weights implicitly) can follow a generic continuous distribution. We can always transform them to a standard normal random variables. Therefore, in an attempt to generalize, we transform the true gap length θ (or $\hat{\theta}$), hydrostatic heads $h_{\text{up}}, h_{\text{down}}$, and the noise ζ_i into their respective standard normal forms denoted by a tilde $\tilde{(\cdot)}$ over the respective quantity. Since the hydrostatic heads and noise for the i^{th} strain gauge is Gaussian in our case, their standard normal forms can be written as $\tilde{h}_{\text{up}}$, and $\tilde{h}_{\text{down}}$, such that $h_{\text{up}} = \tilde{h}_{\text{up}}\sigma_{h_{\text{up}}} + \mu_{h_{\text{up}}}, h_{\text{down}} = \tilde{h}_{\text{down}}\sigma_{h_{\text{down}}} + \mu_{h_{\text{down}}}$, and $\varepsilon_i = \tilde{\varepsilon}_i\sigma_{\varepsilon_i} + \mu_{\varepsilon_i}$, where $\tilde{h}_{\text{up}}, \tilde{h}_{\text{down}}$ and $\tilde{\varepsilon}_i$ are the realizations of standard normal random variables $\tilde{H}_{\text{up}}, \tilde{H}_{\text{down}}$, and $\tilde{\zeta}_i$ respectively. We transform the prior $f_\Theta(\theta)$ and the modified prior $f_{\hat{\Theta}}\left(\hat{\theta}\right)$ to a *standard normal* random variable $\tilde{\Theta}$ and $\tilde{\hat{\Theta}}$ respectively, such that the cumulative density functions are equal: $F_\Theta(\theta) = F_{\tilde{\Theta}}\left(\tilde{\theta}\right)$, and $F_{\hat{\Theta}}\left(\hat{\theta}\right) = F_{\tilde{\hat{\Theta}}}\left(\tilde{\hat{\theta}}\right)$. This transforms ξ_e into a joint standard normal random variable $\tilde{\xi}_e$ (with a realization $\tilde{\beta}_e$), such that

$$\begin{aligned} &f_{\tilde{\xi}_e}\left(\tilde{\beta}_e\right) = f_{\tilde{H}_{\text{up}}}\left(\tilde{h}_{\text{up}}\right).f_{\tilde{H}_{\text{down}}}\left(\tilde{h}_{\text{down}}\right).\prod_{i=1}^{N_{\text{sg}}(e)} f_{\tilde{\zeta}_i}(\tilde{\varepsilon}_i), \quad \text{where,} \\ &\tilde{\beta}_e = \left(\tilde{h}_{\text{up}}, \tilde{h}_{\text{down}}, \tilde{\varepsilon}_1, \tilde{\varepsilon}_2, \cdots, \tilde{\varepsilon}_{N_{\text{sg}}(e)}\right). \end{aligned} \tag{31}$$

We can now rewrite Bayes risk in Eq. (24) as:

$$\mathfrak{E}_{\text{explicit-risk}}(e) = E_{\tilde{\Theta}\tilde{\xi}_e}\left[\tilde{\mathscr{L}}\left(\tilde{\theta}, \tilde{\beta}_e\right)\right], \quad \text{where,} \quad \tilde{\mathscr{L}}\left(\tilde{\theta}, \tilde{\beta}_e\right) = \mathscr{L}(\theta, \beta_e); \tag{32a}$$

$$\mathfrak{E}_{\text{implicit-risk}}(e) = E_{\tilde{\hat{\Theta}}\tilde{\xi}_e}\left[\tilde{\mathscr{D}}_f\left(\tilde{\hat{\theta}}, \tilde{\beta}_e\right)\right], \quad \text{where,} \quad \tilde{\mathscr{D}}_f\left(\tilde{\hat{\theta}}, \tilde{\beta}_e\right) = \mathscr{D}_f\left(\hat{\theta}, \beta_e\right). \tag{32b}$$

The next section approximates the Bayes risk defined in Eq. (32) by using univariate dimensional reduction and Gauss-Hermite quadrature to carry out the integration.

4.2. Univariate dimensional reduction and Gauss-Hermite quadrature

To obtain the optimal sensor placement design, we may either optimize $\mathfrak{E}_{\text{explicit}-\text{risk}}(e)$ or $\mathfrak{E}_{\text{implicit}-\text{risk}}(e)$. Since these are both integrals, we will use Gauss-Hermite quadrature to approximate the Bayes risk. In this section, we in parallel detail the numerical approximation of $\mathfrak{E}_{\text{explicit}-\text{risk}}(e)$ or $\mathfrak{E}_{\text{implicit}-\text{risk}}(e)$. Recall that the vector $\tilde{\beta}_e$ consists of $(N_{\text{sg}}(e)+2)$ variables. To catalyze the derivation to estimate the Bayes risk using univariate dimensional reduction and Gauss-Hermite quadrature, we define the following spaces

$$\Omega_{\tilde{\Psi}_e} = \Omega_{\tilde{\Theta}} \times \Omega_{\tilde{\xi}_e}, \quad \text{such that} \quad \tilde{\psi}_e = \left(\tilde{\theta}, \tilde{\beta}_e\right) = \left(\tilde{\theta}, \tilde{h}_{\text{up}}, \tilde{h}_{\text{down}}, \tilde{\varepsilon}_1, \tilde{\varepsilon}_2, \cdots, \tilde{\varepsilon}_{N_{\text{sg}}(e)}\right) \in \Omega_{\tilde{\Psi}_e} \tag{33a}$$

$$\Omega_{\tilde{\tilde{\Psi}}_e} = \Omega_{\tilde{\tilde{\Theta}}} \times \Omega_{\tilde{\xi}_e}, \quad \text{such that} \quad \tilde{\tilde{\psi}}_e = \left(\tilde{\tilde{\theta}}, \tilde{\beta}_e\right) = \left(\tilde{\tilde{\theta}}, \tilde{h}_{\text{up}}, \tilde{h}_{\text{down}}, \tilde{\varepsilon}_1, \tilde{\varepsilon}_2, \cdots, \tilde{\varepsilon}_{N_{\text{sg}}(e)}\right) \in \Omega_{\tilde{\tilde{\Psi}}_e} \tag{33b}$$

To distinguish between a variable with or without the hat $\tilde{(\cdot)}$, refer to Eq. (25) for the definition of transformed gap length $\hat{\theta}$ used in the expression of implicit-risk Bayes risk. Equation set (33) allows us to write the Bayes risk in a more desirable form

$$\mathfrak{E}_{\text{explicit}-\text{risk}}(e) = E_{\tilde{\Psi}_e}\left[\tilde{\mathscr{L}}\left(\tilde{\psi}_e\right)\right] = \int_{\Omega_{\tilde{\Psi}_e}} f_{\tilde{\Psi}_e}\left(\tilde{\psi}_e\right)\tilde{\mathscr{L}}\left(\tilde{\psi}_e\right)\mathrm{d}\tilde{\psi}_e, \quad \text{where,} \quad \tilde{\mathscr{L}}\left(\tilde{\psi}_e\right) = \tilde{\mathscr{L}}\left(\tilde{\theta}, \tilde{\beta}_e\right). \tag{34a}$$

$$\mathfrak{E}_{\text{implicit}-\text{risk}}(e) = E_{\tilde{\tilde{\Psi}}_e}\left[\tilde{\mathscr{D}}_f\left(\tilde{\tilde{\psi}}_e\right)\right] = \int_{\Omega_{\tilde{\tilde{\Psi}}_e}} f_{\tilde{\tilde{\Psi}}_e}\left(\tilde{\tilde{\psi}}_e\right)\tilde{\mathscr{D}}_f\left(\tilde{\tilde{\psi}}_e\right)\mathrm{d}\tilde{\tilde{\psi}}_e, \text{where,} \tilde{\mathscr{D}}_f\left(\tilde{\tilde{\psi}}_e\right) = \tilde{\mathscr{D}}_f\left(\tilde{\tilde{\theta}}, \tilde{\beta}_e\right). \tag{34b}$$

Like Figs. 5 and 6 illustrates a function or a module called "*Evaluate the Utility* $\tilde{\mathscr{L}}\left(\tilde{\theta}, \tilde{\beta}_e\right)$" and "*Evaluate the f-divergence* $\tilde{\mathscr{D}}_f\left(\tilde{\tilde{\theta}}, \tilde{\beta}_e\right)$" that obtains the utility $\tilde{\mathscr{L}}\left(\tilde{\psi}_e\right)$ or the f-divergence $\tilde{\mathscr{D}}_f\left(\tilde{\tilde{\psi}}_e\right)$ for a given design e and the input variables $\left(\tilde{\theta}, \tilde{\beta}_e\right)$ or $\left(\tilde{\tilde{\theta}}, \tilde{\beta}_e\right)$ respectively. The module "*Evaluate the Utility* $\tilde{\mathscr{L}}\left(\tilde{\theta}, \tilde{\beta}_e\right)$" is required to evaluate $\mathfrak{E}_{\text{explicit}-\text{risk}}(e)$, and the module "*Evaluate the f-divergence* $\tilde{\mathscr{D}}_f\left(\tilde{\tilde{\psi}}_e\right)$" is required to evaluate $\mathfrak{E}_{\text{implicit}-\text{risk}}(e)$. It does so by transforming the standard-normal variables back to their original form, i.e., $\left(\tilde{\theta}, \tilde{\beta}_e\right) \longrightarrow (\theta, \beta_e)$ or $\left(\tilde{\tilde{\theta}}, \tilde{\beta}_e\right) \longrightarrow \left(\hat{\theta}, \beta_e\right)$, and then using the module "*Evaluate the Utility* $\mathscr{L}(\theta, \beta_e)$" or "*Evaluate the f-divergence* $\mathscr{D}_f\left(\hat{\theta}, \beta_e\right)$" (illustrated in Fig. 5)) to obtain the respective quantities.

The integrals in Eqs. (34a) and (34a) are high dimensional expectations in $(N_{\text{sg}}(e)+3)$ dimensional spaces, making classic multivariate quadrature rules (e.g., quasi Monte Carlo or Smolyak sparse grids) prohibitively expensive. Monte Carlo

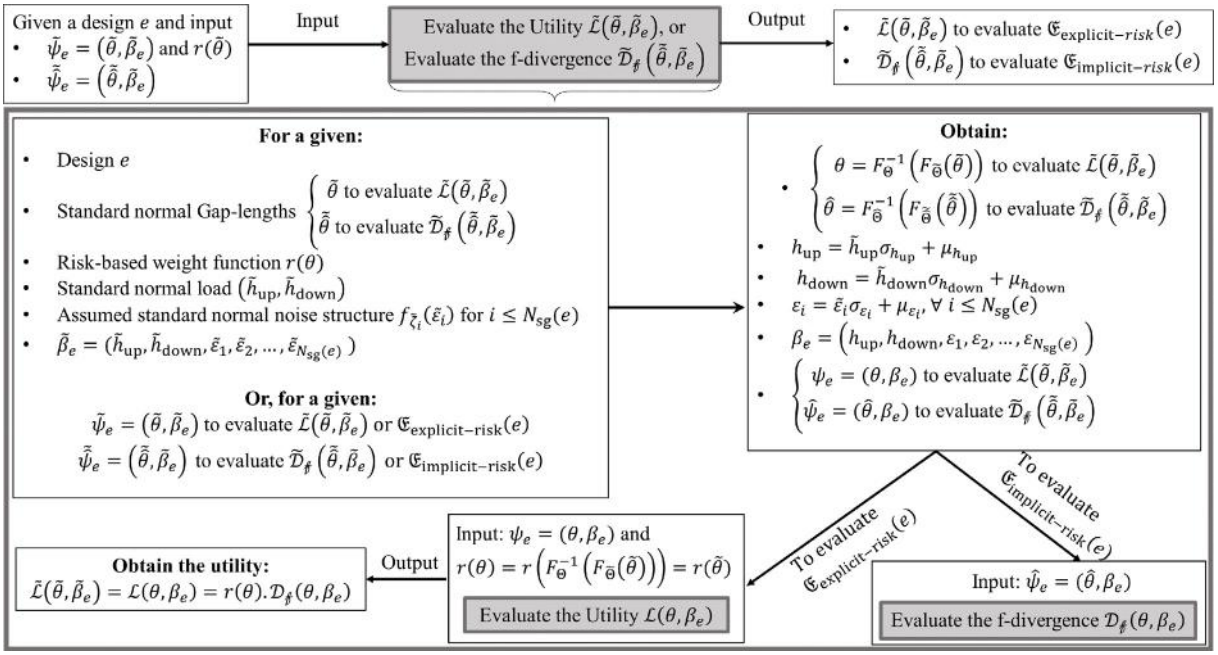

Fig. 6. Evaluating the utility $\tilde{\mathscr{L}}\left(\tilde{\psi}_e\right) = \tilde{\mathscr{L}}\left(\tilde{\theta}, \tilde{\beta}_e\right)$ or the f-divergence $\tilde{\mathscr{D}}_f\left(\tilde{\tilde{\psi}}_e\right) = \tilde{\mathscr{D}}_f\left(\tilde{\tilde{\theta}}, \tilde{\beta}_e\right)$ for a given $\left(\tilde{\theta}, \tilde{\beta}_e\right)$, or $\left(\tilde{\tilde{\theta}}, \tilde{\beta}_e\right)$, respectively.

approximations converge slowly and require a large number of samples to approximate the expectations. This is problematic because an expensive Bayesian inference problem needs to be solved to evaluate the integrands in Eqs. (34a) and (34a). To overcome these issues, we employ an approximation to the integrals in Eqs. (34a) and (34a) based on *univariate dimension reduction*. To do so, we define the following vectors, each consisting of $(N_{\text{sg}}(e)+3)$ components:

$$\begin{aligned}
\tilde{\psi}_0 &= (0,0,0,0,0,\cdots,0);\\
\tilde{\psi}_1 &= \left(\tilde{\theta},0,0,0,0,\cdots,0\right);\\
\tilde{\psi}_2 &= \left(0,\tilde{h}_{\text{up}},0,0,0,\cdots,0\right);\\
\tilde{\psi}_3 &= \left(0,0,\tilde{h}_{\text{down}},0,0,\cdots,0\right);\\
\tilde{\psi}_4 &= (0,0,0,\tilde{\varepsilon}_1,0,\cdots,0);\\
\tilde{\psi}_5 &= (0,0,0,0,\tilde{\varepsilon}_2,\cdots,0);\\
&\vdots\\
\tilde{\psi}_{\left(N_{\text{sg}}(e)+3\right)} &= \left(0,0,0,0,0,\cdots,\tilde{\varepsilon}_{N_{\text{sg}}(e)}\right).
\end{aligned} \tag{35}$$

$$\begin{aligned}
\tilde{\tilde{\psi}}_0 &= (0,0,0,0,0,\cdots,0);\\
\tilde{\tilde{\psi}}_1 &= \left(\tilde{\tilde{\theta}},0,0,0,0,\cdots,0\right);\\
\tilde{\tilde{\psi}}_2 &= \left(0,\tilde{h}_{\text{up}},0,0,0,\cdots,0\right);\\
\tilde{\tilde{\psi}}_3 &= \left(0,0,\tilde{h}_{\text{down}},0,0,\cdots,0\right);\\
\tilde{\tilde{\psi}}_4 &= (0,0,0,\tilde{\varepsilon}_1,0,\cdots,0);\\
\tilde{\tilde{\psi}}_5 &= (0,0,0,0,\tilde{\varepsilon}_2,\cdots,0);\\
&\vdots\\
\tilde{\tilde{\psi}}_{\left(N_{\text{sg}}(e)+3\right)} &= \left(0,0,0,0,0,\cdots,\tilde{\varepsilon}_{N_{\text{sg}}(e)}\right).
\end{aligned} \tag{36}$$

Note that $\tilde{\psi}_i$ are exactly same as $\tilde{\tilde{\psi}}_i$ except for $i=1$. Using the definitions above and *univariate dimensional reduction* (refer to [32]), we approximate the utility function $\tilde{\mathscr{L}}\left(\tilde{\psi}_e\right)$ or the f-divergence $\tilde{\mathscr{D}}_f\left(\tilde{\tilde{\psi}}_e\right)$ as:

$$\tilde{\mathscr{L}}\left(\tilde{\psi}_e\right) \approx -\left(N_{\text{sg}}(e)+2\right)\tilde{\mathscr{L}}\left(\tilde{\psi}_0\right) + \sum_{i=1}^{\left(N_{\text{sg}}(e)+3\right)} \tilde{\mathscr{L}}\left(\tilde{\psi}_i\right); \tag{37a}$$

$$\tilde{\mathscr{D}}_f\left(\tilde{\tilde{\psi}}_e\right) \approx -\left(N_{\text{sg}}(e)+2\right)\tilde{\mathscr{D}}_f\left(\tilde{\tilde{\psi}}_0\right) + \sum_{i=1}^{\left(N_{\text{sg}}(e)+3\right)} \tilde{\mathscr{D}}_f\left(\tilde{\tilde{\psi}}_i\right). \tag{37b}$$

Substituting Eq. (37a) into Eq. (32a), we get,

$$\begin{aligned}
\mathfrak{E}_{\text{explicit}-\text{risk}}(e) &\approx -\left(N_{\text{sg}}(e)+2\right)E_{\tilde{\Psi}_e}\left[\tilde{\mathscr{L}}\left(\tilde{\psi}_0\right)\right] + \sum_{i=1}^{\left(N_{\text{sg}}(e)+3\right)} E_{\tilde{\Psi}_e}\left[\tilde{\mathscr{L}}\left(\tilde{\psi}_i\right)\right]\\
&= -\left(N_{\text{sg}}(e)+2\right)\int_{\Omega_{\tilde{\Psi}_e}} f_{\tilde{\Psi}_e}\left(\tilde{\psi}_e\right)\tilde{\mathscr{L}}\left(\tilde{\psi}_0\right)\mathrm{d}\tilde{\psi}_e + \sum_{i=1}^{\left(N_{\text{sg}}(e)+3\right)}\int_{\Omega_{\tilde{\Psi}_e}} f_{\tilde{\Psi}_e}\left(\tilde{\psi}_e\right)\tilde{\mathscr{L}}\left(\tilde{\psi}_i\right)\mathrm{d}\tilde{\psi}_e\\
&= -\left(N_{\text{sg}}(e)+2\right)\tilde{\mathscr{L}}\left(\tilde{\psi}_0\right) + \sum_{i=1}^{\left(N_{\text{sg}}(e)+3\right)}\int_{\Omega_{\tilde{\Psi}_e}} f_{\tilde{\Psi}_e}\left(\tilde{\psi}_e\right)\tilde{\mathscr{L}}\left(\tilde{\psi}_i\right)\mathrm{d}\tilde{\psi}_e.
\end{aligned} \tag{38}$$

Similarly, substituting Eq. (37b) into Eq. (32b), we get,

$$\mathfrak{E}_{\text{implicit}-\text{risk}}(e) \approx -\left(N_{\text{sg}}(e)+2\right)\tilde{\mathscr{D}}_f\left(\tilde{\tilde{\psi}}_0\right) + \sum_{i=1}^{\left(N_{\text{sg}}(e)+3\right)}\int_{\Omega_{\tilde{\tilde{\Psi}}_e}} f_{\tilde{\tilde{\Psi}}_e}\left(\tilde{\tilde{\psi}}_e\right)\tilde{\mathscr{D}}_f\left(\tilde{\tilde{\psi}}_i\right)\mathrm{d}\tilde{\tilde{\psi}}_e. \tag{39}$$

To simplify the expression above, firstly, we realize that $f_{\tilde{\Psi}_e}\left(\tilde{\psi}_e\right)$ and $f_{\tilde{\tilde{\Psi}}_e}\left(\tilde{\tilde{\psi}}_e\right)$ are the joint probability density function of statistically-independent standard normal random variables. Therefore,

$$f_{\tilde{\Psi}_e}\left(\tilde{\psi}_e\right) = f_{\tilde{\Theta}}\left(\tilde{\theta}\right).f_{\tilde{\zeta}_e}\left(\tilde{\beta}_e\right) = f_{\tilde{\Theta}}\left(\tilde{\theta}\right).f_{H^{\sim}_{\text{up}}}\left(\tilde{h}_{\text{up}}\right).f_{H^{\sim}_{\text{down}}}\left(\tilde{h}_{\text{down}}\right).\prod_{i=1}^{N_{\text{sg}}(e)} f_{\tilde{\zeta}_i}(\tilde{\varepsilon}_i); \tag{40a}$$

$$f_{\tilde{\tilde{\Psi}}_e}\left(\tilde{\tilde{\psi}}_e\right) = f_{\tilde{\tilde{\Theta}}}\left(\tilde{\tilde{\theta}}\right).f_{\tilde{\tilde{\zeta}}_e}\left(\tilde{\tilde{\beta}}_e\right) = f_{\tilde{\tilde{\Theta}}}\left(\tilde{\tilde{\theta}}\right).f_{H^{\sim}_{\text{up}}}\left(\tilde{h}_{\text{up}}\right).f_{H^{\sim}_{\text{down}}}\left(\tilde{h}_{\text{down}}\right).\prod_{i=1}^{N_{\text{sg}}(e)} f_{\tilde{\zeta}_i}(\tilde{\varepsilon}_i). \tag{40b}$$

Since all these random variables are standard normal, using the notation defined in Eq. (1) we can re-write Eq. (40) in a more desirable form as:

$$f_{\tilde{\Psi}_e}\left(\tilde{\psi}_e\right) = \phi\left(\tilde{\theta}\right).\phi\left(\tilde{h}_{\text{up}}\right).\phi\left(\tilde{h}_{\text{down}}\right).\prod_{i=1}^{N_{\text{sg}}(e)}\phi(\tilde{\varepsilon}_i) = \prod_{i=1}^{N_{\text{sg}}(e)+3}\phi\left(\tilde{b}_i\right) = \prod_{i=1}^{N_{\text{sg}}(e)+3}\left(\frac{1}{\sqrt{2\pi}}e^{-\frac{1}{2}\tilde{b}_i^2}\right); \tag{41a}$$

$$f_{\tilde{\tilde{\Psi}}_e}\left(\tilde{\tilde{\psi}}_e\right) = \phi\left(\tilde{\tilde{\theta}}\right).\phi\left(\tilde{h}_{\text{up}}\right).\phi\left(\tilde{h}_{\text{down}}\right).\prod_{i=1}^{N_{\text{sg}}(e)}\phi(\tilde{\varepsilon}_i) = \prod_{i=1}^{N_{\text{sg}}(e)+3}\phi\left(\tilde{\tilde{b}}_i\right) = \prod_{i=1}^{N_{\text{sg}}(e)+3}\left(\frac{1}{\sqrt{2\pi}}e^{-\frac{1}{2}\tilde{\tilde{b}}_i^2}\right). \tag{41b}$$

In the equation above, $\tilde{b}_1 = \tilde{\theta}, \tilde{b}_2 = \tilde{h}_{\text{up}}, \tilde{b}_3 = \tilde{h}_{\text{down}}$ and $\tilde{b}_{j+3} = \tilde{\varepsilon}_j$, for $j \in (1, 2, \cdots, N_{\text{sg}}(e))$, with $\Omega_{\tilde{b}_i}$ representing the respective space (for example: $\Omega_{\tilde{b}_1} = \Omega_{\tilde{\Theta}}$). Similarly, $\tilde{\tilde{b}}_1 = \tilde{\tilde{\theta}}, \tilde{\tilde{b}}_2 = \tilde{h}_{\text{up}}, \tilde{\tilde{b}}_3 = \tilde{h}_{\text{down}}$ and $\tilde{\tilde{b}}_{j+3} = \tilde{\tilde{\varepsilon}}_j$, for $j \in (1, 2, \cdots, N_{\text{sg}}(e))$, with $\Omega_{\tilde{\tilde{b}}_i}$ representing the respective space (for example: $\Omega_{\tilde{\tilde{b}}_1} = \Omega_{\tilde{\tilde{\Theta}}}$). Secondly, we note that for any function of the form $g(x \in X, y = 0 \in Y), E_{XY}(g(x,0)) = E_X(g(x,0))$, provided X and Y are statistically-independent random variables. This allows us to simplify the integral in Eq. (38) and (39) as:

$$\int_{\Omega_{\tilde{\Psi}_e}} f_{\tilde{\Psi}_e}\left(\tilde{\psi}_e\right)\tilde{\mathscr{L}}\left(\tilde{\psi}_i\right)\mathrm{d}\tilde{\psi}_e = \frac{1}{\sqrt{2\pi}}\int_{\Omega_{\tilde{b}_i}}\tilde{\mathscr{L}}\left(\tilde{\psi}_i\right)e^{-\frac{1}{2}\tilde{b}_i^2}\mathrm{d}\tilde{b}_i; \tag{42a}$$

$$\int_{\Omega_{\tilde{\tilde{\Psi}}_e}} f_{\tilde{\tilde{\Psi}}_e}\left(\tilde{\tilde{\psi}}_e\right)\tilde{\mathscr{D}}_f\left(\tilde{\tilde{\psi}}_i\right)\mathrm{d}\tilde{\tilde{\psi}}_e = \frac{1}{\sqrt{2\pi}}\int_{\Omega_{\tilde{\tilde{b}}_i}}\tilde{\mathscr{D}}_f\left(\tilde{\tilde{\psi}}_i\right)e^{-\frac{1}{2}\tilde{\tilde{b}}_i^2}\mathrm{d}\tilde{\tilde{b}}_i. \tag{42b}$$

We realize that the Gauss-Hermite quadrature is a natural choice for approximating the integrals in the equation above. This is because Gauss-Hermite quadrature is meant to estimate integrals of the form $\int_x g(x)e^{-x^2}\mathrm{d}x$, for any function $g(x)$. Therefore, the approximations are

$$\int_{\Omega_{\tilde{\Psi}_e}} f_{\tilde{\Psi}_e}\left(\tilde{\psi}_e\right)\tilde{\mathscr{L}}\left(\tilde{\psi}_i\right)\mathrm{d}\tilde{\psi}_e \approx \frac{1}{\sqrt{\pi}}\sum_{n=1}^{\natural}\omega_n\tilde{\mathscr{L}}(\tilde{q}_{i,n}), \quad \text{where} \quad \tilde{q}_{i,n}(j) = \begin{cases}\tilde{\psi}_i(j) = 0 & i \neq j;\\ \alpha_n & i = j.\end{cases} \tag{43a}$$

$$\int_{\Omega_{\tilde{\tilde{\Psi}}_e}} f_{\tilde{\tilde{\Psi}}_e}\left(\tilde{\tilde{\psi}}_e\right)\tilde{\mathscr{D}}_f\left(\tilde{\tilde{\psi}}_i\right)\mathrm{d}\tilde{\tilde{\psi}}_e \approx \frac{1}{\sqrt{\pi}}\sum_{n=1}^{\natural}\omega_n\tilde{\mathscr{D}}_f\left(\tilde{\tilde{q}}_{i,n}\right), \quad \text{where} \quad \tilde{\tilde{q}}_{i,n}(j) = \begin{cases}\tilde{\tilde{\psi}}_i(j) = 0 & i \neq j;\\ \alpha_n & i = j.\end{cases} \tag{43b}$$

In the equations above, $\tilde{q}_{i,n}(j)$ (or $\tilde{\tilde{\psi}}_i(j)$) represents the j^{th} component of the vector $\tilde{q}_{i,n}$ (or $\tilde{\tilde{\psi}}_i$); $\natural$ represents quadrature order; ω_n gives the weights; and α_n gives the point of evaluation of the function for $n \leqslant \natural$. For our calculations, we use $\natural = 3$, for which $\omega_1 = \frac{2}{3}\sqrt{\pi}, \omega_2 = \frac{1}{6}\sqrt{\pi}, \omega_3 = -\frac{1}{6}\sqrt{\pi}, \alpha_1 = 0, \alpha_2 = \frac{\sqrt{6}}{2}$, and $\alpha_3 = -\frac{\sqrt{6}}{2}$. This choice of the quadrature order satisfies the computational accuracy that this problem demands and at the same time leads to a computationally efficient numerical estimation of Bayes risk. The approximated Bayes risk functions can now be written as

$$\mathfrak{E}_{\text{explicit}-\text{risk}}(e) \approx -(N_{\text{sg}}(e)+2)\tilde{\mathscr{L}}\left(\tilde{\psi}_0\right) + \sum_{i=1}^{(N_{\text{sg}}(e)+3)}\sum_{n=1}^{\natural=3}\omega_n\tilde{\mathscr{L}}(\tilde{q}_{i,n}); \tag{44a}$$

$$\mathfrak{E}_{\text{implicit}-\text{risk}}(e) \approx -(N_{\text{sg}}(e)+2)\tilde{\mathscr{D}}_f\left(\tilde{\tilde{\psi}}_0\right) + \sum_{i=1}^{(N_{\text{sg}}(e)+3)}\sum_{n=1}^{\natural=3}\omega_n\tilde{\mathscr{D}}_f\left(\tilde{\tilde{q}}_{i,n}\right). \tag{44b}$$

Fig. 7 illustrates the algorithmic flowchart to obtain the explicit and implicit form of Bayes risk functional defined in Eq. (44).

As was noted in Eq. (27) that, mathematically, optimization using explicit and implicit Bayes risk functional should yield the same result. However, since we numerically estimate $\mathfrak{E}_{\text{explicit}-\text{risk}}(e)$ and $\mathfrak{E}_{\text{implicit}-\text{risk}}(e)$ using Gauss-Hermite quadrature in conjuncture with univariate dimensional reduction, optimization using these functional leads to a different sensor designs. This is because evaluating $\mathfrak{E}_{\text{explicit}-\text{risk}}(e)$ requires using observed strain measurements corresponding to the gap length values $\theta = F_{\Theta}^{-1}\left(F_{\tilde{\Theta}}\left(\tilde{\theta} = \alpha_n\right)\right)$, whereas evaluating $\mathfrak{E}_{\text{implicit}-\text{risk}}(e)$ requires using a different set of observed strain measured corresponding to the true gap length values $\tilde{\theta} = F_{\tilde{\Theta}}^{-1}\left(F_{\tilde{\Theta}}\left(\tilde{\tilde{\theta}} = \alpha_n\right)\right)$. In other words, since the cumulative distribution functions $F_{\tilde{\Theta}}\left(\tilde{\theta}\right)$ (obtained from the prior distribution of gap length) and $F_{\tilde{\tilde{\Theta}}}\left(\tilde{\tilde{\theta}}\right)$ (obtained from the modified prior distribution of

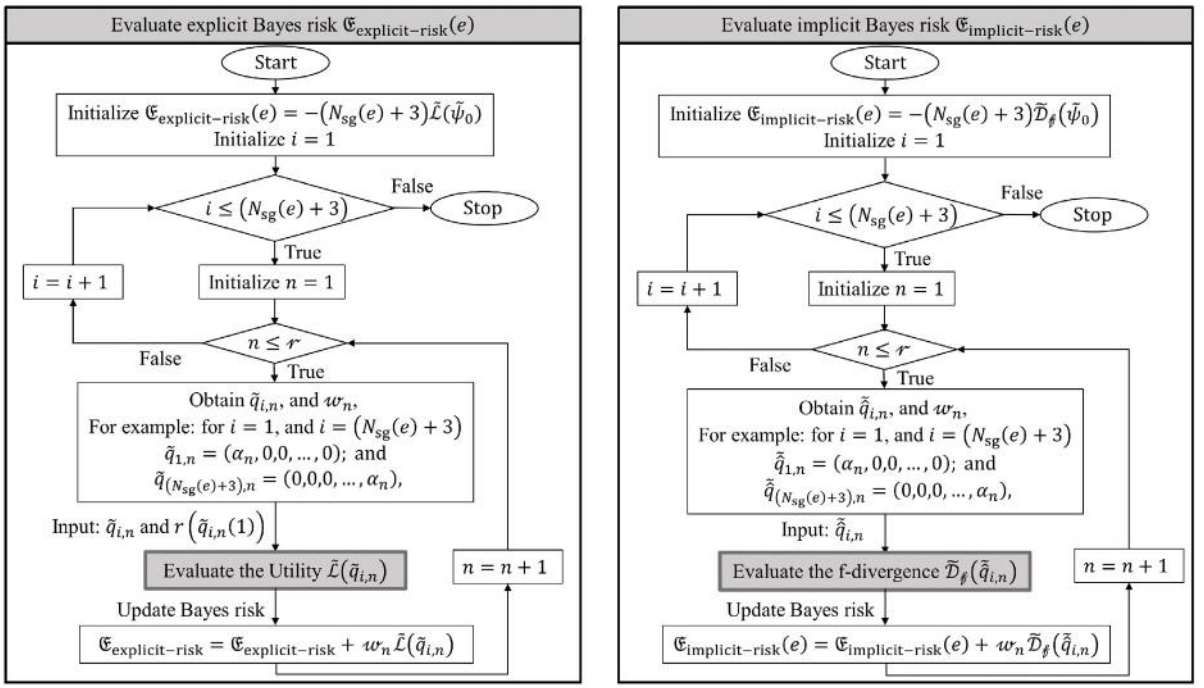

Fig. 7. Algorithm to evaluate both the explicit and implicit Bayes risk.

gap length) are different, the Gauss point α_n maps to a different values of true gap lengths θ and $\tilde{\theta}$, and hence requires using different simulated strain data. We use implicit Bayes risk as the objective functional because it shows the effect of risk-weights more prominently than obtained using the explicit Bayes risk.

It is natural to address the question *"How many times do we need to run the GPR model to obtain the Bayes risk* $\mathfrak{E}_{\text{explicit-risk}}(e)$ *or* $\mathfrak{E}_{\text{implicit-risk}}(e)$ *defined by* Eq. (44) *for a single design consideration e?*" We show the calculation for the explicit Bayes risk and note that the number of GPR runs are the same for explicit or implicit Bayes risk functional evaluation. To start with, we realize that there are two sums in the expression of $\mathfrak{E}_{\text{explicit-risk}}(e)$ in Eq. (44). Therefore, the cost function $\tilde{\mathscr{L}}(\tilde{q}_{i,n})$ has to be obtained $r.(N_{sg}(e)+3)$ times for all the possible $\tilde{q}_{i,n}$, where $i \leqslant (N_{sg}(e)+3)$ and $n \leqslant r$. For a fixed value of the index i and n, the vector $\tilde{q}_{i,n}$ consist of some realization of the standard-normal quantities $\left(\tilde{\theta}, \tilde{\beta}_e\right)$ obtained by Eq. (43). From Remark 3, obtaining the utility function $\tilde{\mathscr{L}}(\tilde{q}_{i,n})$ for a fixed $\tilde{q}_{i,n}$ requires running the GPR model $(N_{\text{particles}}+1)$ times. It can also be seen in the Fig. 7 that the utility $\tilde{\mathscr{L}}(\tilde{q}_{i,n})$ is evaluated for every $\tilde{q}_{i,n}$ by calling a function "*Expected the Utility* $\tilde{\mathscr{L}}(\tilde{q}_{i,n})$" that requires running GPR model $(N_{\text{particles}}+1)$ times at every instance the function is called (refer to Fig. 5). Therefore, evaluating Bayes risk using Eq. (44) for a given design e requires running the GPR model N_{GPR1} times, such that:

$$N_{\text{GPR1}} = r \times (N_{\text{particles}}+1) \times (N_{sg}(e)+3). \tag{45}$$

These GPR model runs make evaluating Bayes risk computationally expensive.

Bayesian optimization aimed at obtaining the optimal sensor network design consists of evaluating many such designs, denoted by e_i, consisting of $N_{sg}(e_i)$ number of sensors. To obtain an optimized sensor placement design, we start with an initially assumed design, denoted by e_0, that consists of $N_{sg}(e_0)$ number of sensors. Starting with e_0, the subsequent sensor design e_i with $N_{sg}(e_i)$ sensors is obtained by picking the most optimal sensor location from the available sensors and adding that sensor location to the previous design e_{i-1} with $N_{sg}(e_{i-1}) = N_{sg}(e_i) - 1$ sensors. Picking the additional sensor required to update the design e_{i-1} to the design e_i requires $N_{\text{iter}}(e_i)$ number of iterations. Since Bayes risk is the optimiality criteria, it needs to be evaluated at every iteration for the design e_i. Let e_I, with $i = I$, represent the final optimal sensor network design. The total number of GPR runs to arrive at e_I (starting from e_0) is denoted by N_{GPR2}, such that:

$$N_{\text{GPR2}} = \sum_{i=1}^{I} r \times (N_{\text{particles}}+1) \times (N_{sg}(e_i)+3) \times N_{\text{iter}}(e_i). \tag{46}$$

So far, we have taken two major steps to reduce the computational cost. First, we have used a digital surrogate (GPR) of the finite element model. Secondly, we have used SVD to reduce the dimension of the GPR model's output. In the next section,

we propose a novel and innovative approach to further minimize the computational cost for evaluating the Bayes risk by minimizing the number of times we run the GPR model to evaluate the Bayes risk.

4.3. An efficient computational approach to evaluate the Bayes risk

In this section, we highlight the disadvantage of using the algorithm illustrated in Fig. 7 to obtain the explicit and implicit Bayes risk and propose an alternative novel approach that significantly reduces the computational cost of optimization. For the sake of discussion, we consider explicit Bayes risk functional. An approach to evaluate Bayes risk $\mathfrak{E}_{\text{explicit}-\text{risk}}(e)$ for a given design e as illustrated in Fig. 7 involves many repeated evaluation of GPR model $g_e(\theta, h_{\text{up}}, h_{\text{down}})$ for same input arguments $(\theta, h_{\text{up}}, h_{\text{down}})$. The computational cost can be significantly reduced by realizing that in the entire process of evaluating the Bayes risk, there are only $7(N_{\text{particles}}+1)$ unique runs of GPR model. This follows from the following line of reasoning. The vector $\tilde{q}_{i,n}$ is a special case of the vector $\tilde{\psi}_i$ as defined in Eq. (35). The first three components of the vector $\tilde{q}_{i,n}$ constitute a sub-vector $\tilde{q}_{i,n}(1:3) = \left(\tilde{\theta}, \tilde{h}_{\text{up}}, \tilde{h}_{\text{down}}\right)$, the inverse standard-normal transformation of which are the argument of the GPR model $g_e(\theta, h_{\text{up}}, h_{\text{down}}) = \tilde{g}_e\left(\tilde{\theta}, \tilde{h}_{\text{up}}, \tilde{h}_{\text{down}}\right)$. The remaining $N_{\text{sg}}(e)$ components constitute a vector $\tilde{q}_{i,n}(4 : N_{\text{sg}}(e)+3)$ representing external noise. For any vector $\tilde{q}_{i,n}$, the sub-vector $\tilde{q}_{i,n}(1:3) = \left(\tilde{\theta}, \tilde{h}_{\text{up}}, \tilde{h}_{\text{down}}\right)$ bears α_n as numerical value of one of the components and zero for others. Therefore, we have a set of 7 unique sub-vectors $\left(\tilde{\theta}, \tilde{h}_{\text{up}}, \tilde{h}_{\text{down}}\right)$ of interest to us. From remark 1, Figs. 5 and 6, obtaining the utility $\tilde{\mathscr{L}}(\tilde{q}_{i,n})$ for each $\tilde{q}_{i,n}$ requires $(N_{\text{particles}}+1)$ GPR runs. Therefore, considering all the 7 unique arguments of GPR model, we essentially need to run GPR model only N_{GPR3} times, such that:

$$N_{\text{GPR3}} = 7 \times (N_{\text{particles}} + 1). \tag{47}$$

For each of these stand-alone GPR runs, we store the strain values in all the 64919 sensors constituting data of size $7 \times (N_{\text{particles}}+1) \times 64919$ in a matrix called *"strain-data"* and pick the strain measurements of the sensors constituting a design e. Therefore, even while carrying out Bayesian optimization that may consider many designs, the number of GPR runs remains $7 \times (N_{\text{particles}}+1)$ cutting computational cost intensively. Fig. 8 illustrates this process of storing the strain data. Once the matrix *strain-data* is obtained independently, the utility $\tilde{\mathscr{L}}(\tilde{q}_{i,n})$ can be evaluated by extracting the relevant sensor readings from the matrix *strain-data* as demonstrated in Fig. 9. Replacing θ with $\hat{\theta}$, and $\tilde{q}_{i,n}$ with $\hat{\tilde{q}}_{i,n}$ in the flowchart 8 gives the strain-data matrix required to obtain the intrinsic Bayes risk, and replacing them in in the flowchart 9 yields the f-divergence $\tilde{\mathscr{D}}_f\left(\hat{\tilde{\theta}}, \beta_e\right)$ required to obtain the intrinsic Bayes risk.

The modified algorithm to evaluate the Bayes risk $\mathfrak{E}_{\text{explicit}-\text{risk}}(e)$ is illustrated in Fig. 10. The most important difference between the algorithm in Fig. 7 and the one in Fig. 10 is that in the modified algorithm the GPR models are not run at every iteration step.

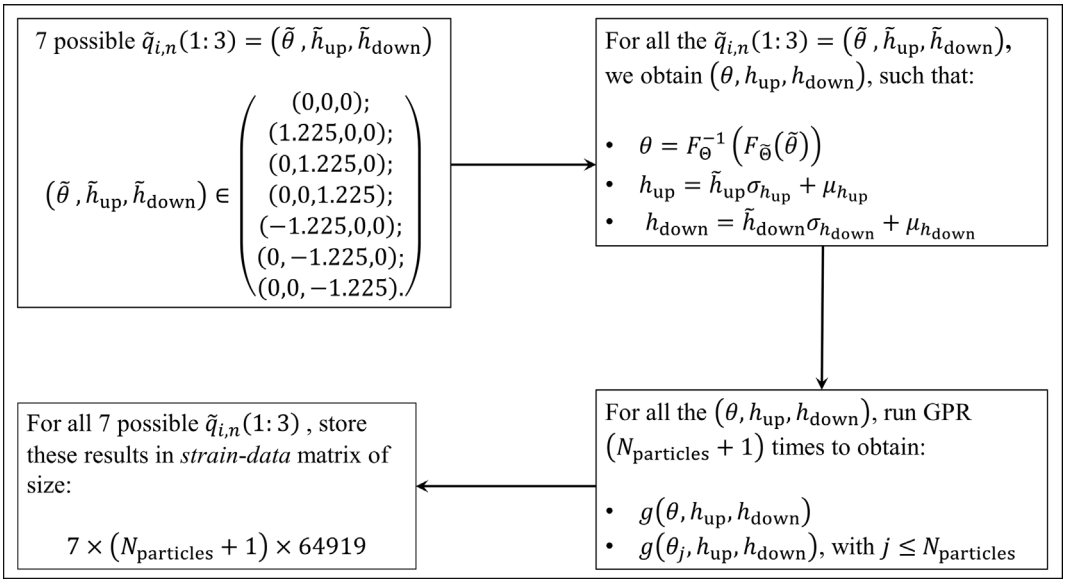

Fig. 8. Obtaining and storing the strain-data required to obtain Bayes risk $\mathfrak{E}_{\text{extrinsic}-\text{risk}}(e)$.

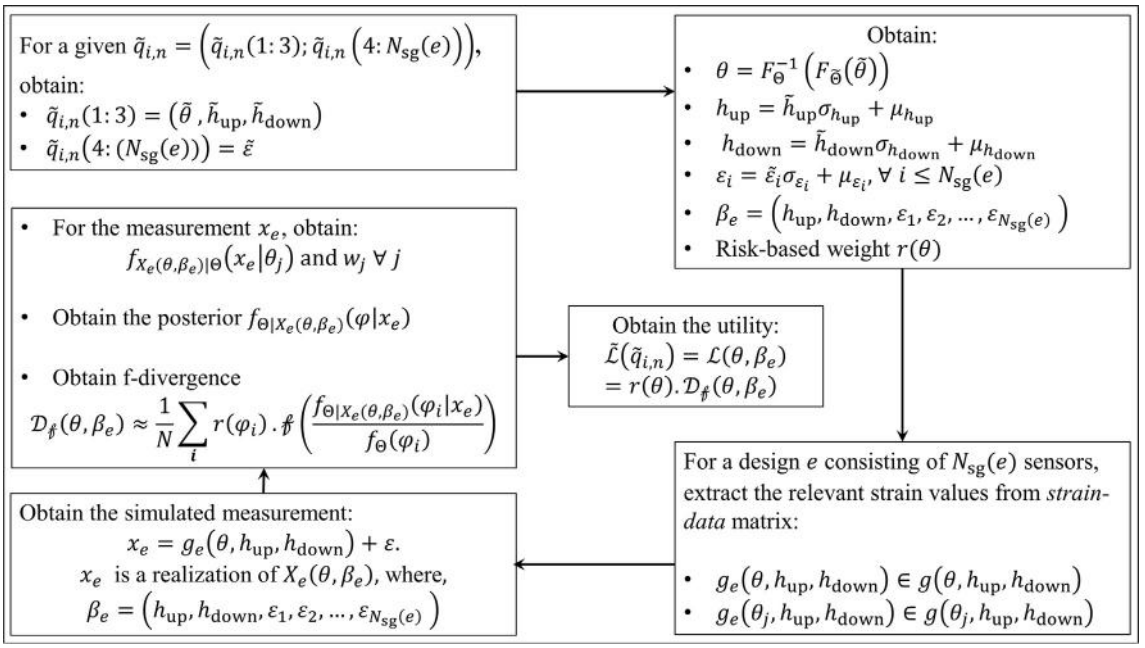

Fig. 9. Obtaining the utility $\tilde{\mathcal{L}}(\tilde{q}_{i,n})$.

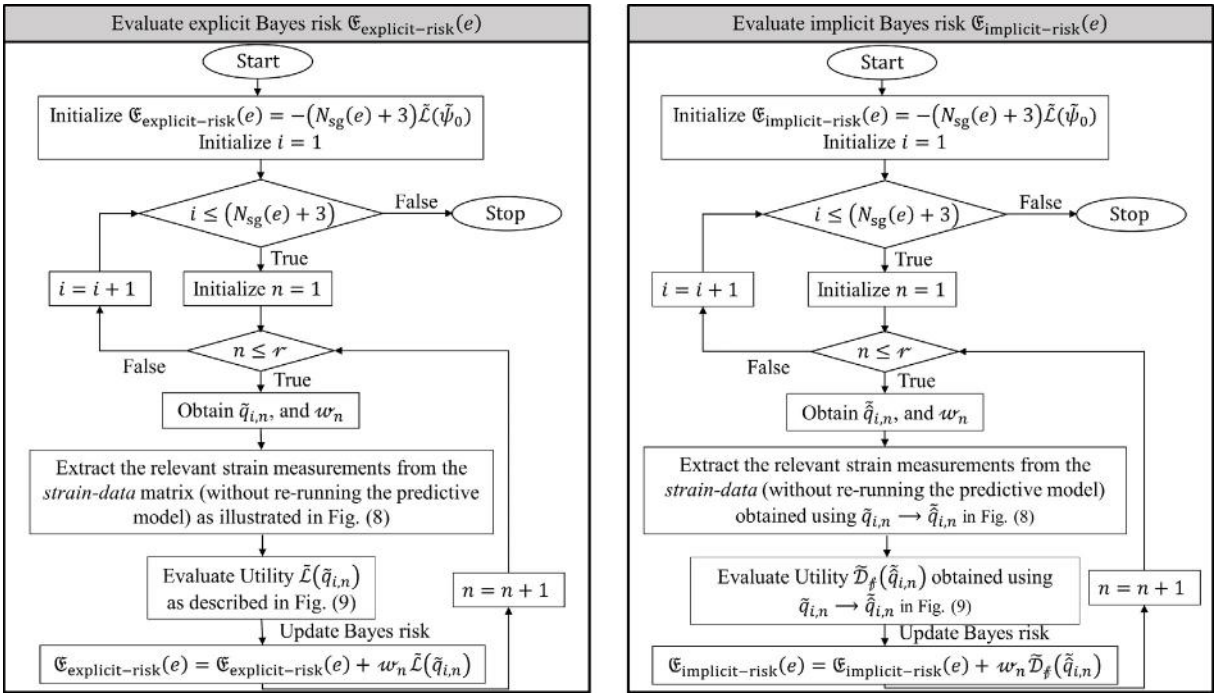

Fig. 10. Computationally efficient algorithm to evaluate the explicit and implicit Bayes risk.

The Fig. 11 compares the number of GPR runs required for Bayesian optimization by considering two approaches used to evaluate Bayes risk as defined in Figs. 7 and 10. Carrying out Bayesian optimization using first approach to evaluate Bayes risk (either extrinsic or intrinsic) Fig. 7 needs N_{GPR2} runs of GPR model that depends on the design e_i considered as defined in Eq. (46). We start by assuming $N_{sg}(e_0) = 3$ number of initial sensors and update the design using up to 10 additional sensors. For simplicity, we assume a constant average number of iterations for each design $N_{iter}(e_i) = 20$. We assume $N_{particles} = 5000$. We observe that number of GPR runs using modified algorithm illustrated in Fig. 10 is $N_{GPR2} = 35007$, which is order of magnitudes smaller as compared to N_{GPR2}. For instance, $N_{GPR2} = 2100420$ for the first additional sensor, and $N_{GPR2} = 34506900$ for ten additional sensors.

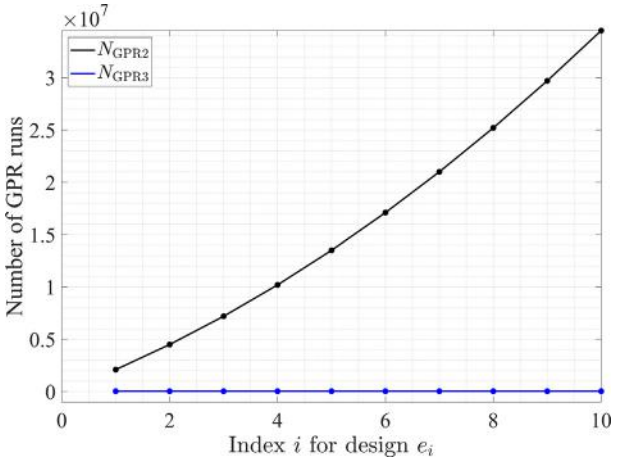

Fig. 11. Number of GPR runs for Bayesian optimization.

5. Bayesian optimization: optimal sensor placement design

5.1. Optimal sensor placement design algorithm

Given that our objective is to find the design e^* that maximizes a Bayes risk functional, we will use the implicit Bayes risk form to solve

$$e^* = \text{argmax}_{e\in\Omega_E}\mathfrak{E}_{\text{implicit-risk}}(e). \tag{48}$$

In general, obtaining e^* involves looking at every possible design combination and choosing the one with the maximum implicit Bayes risk. In our case, where the total number of sensor locations is $n = 64919 \times 4$, this would be choosing e^* from the $\sum_{r=1}^{n}\frac{n!}{r!(n-r)!} = (2^n - 1)$ possible combinations of sensor locations. Therefore, the exhaustive design space Ω_E consists of $\left(2^{259676} - 1\right) \approx 10^{78170}$ possible designs, which is approximately 78090 *orders of magnitude* more than the number of estimated atoms in the universe. Given the intractable nature of exhaustive search, Bayesian optimization is used to look for a global optimum in a minimum number of steps, thus minimizing the sampling points to rapidly speed up the optimization process. Unlike gradient-based optimization methods, Bayesian optimization does not require the derivative of the objective function; having a black-box model (like a surrogate function) of the objective function suffices to perform the optimization. It involves two primary elements. The first element is developing *surrogate function* using another GPR of the objective function using randomly evaluated samples. The second component is the *acquisition function* that helps us locate the next *most valuable* candidate to update the design [33,34].

The process begins by choosing an initial design $e_0 = \left(\mathscr{A}^{(1)}, \mathscr{A}^{(2)}, \cdots, \mathscr{A}^{\left(N_{\text{sg}}(e_0)\right)}\right) \in \Omega_E$ consisting of $N_{\text{sg}}(e_0) = N_0 \geqslant 0$ sensors. Here, $\mathscr{A}^{(l)}$ represents the location of l^{th} strain gauge in the design e_0. The next step is to obtain an updated design e_1 by adding an additional sensor to e_0, such that $N_{\text{sg}}(e_1) = N_0 + 1$. To obtain the optimal e_1, we randomly sample α sensor locations using *Latin Hypercube Sampling* (LHS), subjected to a space filling property, to be the candidate for the additional sensor from the unused sensors constituting the measurement space Ω_X. These locations yield α number of design samples $\tilde{e}_k,\ \forall\, k \leqslant \alpha$ each with $N_{\text{sg}}(e_1)$ sensors. We obtain the exact cost $\mathfrak{E}_{\text{implicit-risk}}(\tilde{e}_k),\ \forall\, k \leqslant \alpha$ using approach discussed in the previous section. Using the set of α additional sensor locations as input data, denoted by $\tilde{\mathscr{A}}$, and the exact cost as output data, we train our surrogate function $\hat{\mathfrak{E}}(\tilde{\mathscr{A}}) \sim N\left(\mu_{\tilde{\mathscr{A}}}, \sigma^2_{\tilde{\mathscr{A}}}\right)$. This surrogate can be used to quickly estimate a posterior probability that describes possible values for the Bayes risk at a remaining candidate location $\bar{\mathscr{A}}$ spanning the entire design space, with mean value $\mu_{\bar{\mathscr{A}}}$ and standard deviation $\sigma_{\bar{\mathscr{A}}}$. We use *Expected Improvement EI* as our acquisition function that helps us locate the next most valuable candidate for the next sensor location based on the current posterior over the Bayes risk, given by

$$EI(\bar{\mathscr{A}}) = \left(\mu_{\bar{\mathscr{A}}} - \mathfrak{E}^*\right)\Phi\left(\frac{\mu_{\bar{\mathscr{A}}} - \mathfrak{E}^*}{\sigma_{\bar{\mathscr{A}}}}\right) + \sigma_{\bar{\mathscr{A}}}\phi\left(\frac{\mu_{\bar{\mathscr{A}}} - \mathfrak{E}^*}{\sigma_{\bar{\mathscr{A}}}}\right). \tag{49}$$

Here, $\mathfrak{E}^* = \max_{\tilde{e}_k}\mathfrak{E}_{\text{implicit-risk}}(\tilde{e}_k)$ is the *current best value* of the objective function. For all the remaining possible additional sensor location candidates, we evaluate $EI(\bar{\mathscr{A}})$. The candidate with maximum *EI* is the next most valuable location. Once we locate the next most valuable sensor location candidate, we get $(\alpha+1)^{\text{th}}$ design samples. We re-train the GPR with $(\alpha+1)$ data points, and keep adding the next most valuable location from the set of strain locations constituting Ω_X until the maximum *EI* is less than a tolerance value ε.

Note that the aforementioned details updates an initial design e_0 to e_1 by adding one additional sensor. We keep updating the designs by adding one sensor at a time until one of the following two conditions is reached:

1. Bayes risk converges to a constant value, i.e., the design $e_I = e^*$ (with $i = I$) can be considered as the most optimal design if $\mathfrak{E}(e_I) \approx \mathfrak{E}(e_{(I-1)})$. Given an updated design $e_i = \left(\mathscr{A}^{(1)}, \mathscr{A}^{(2)}, \cdots, \mathscr{A}^{(N_{sg}(e_i))}\right)$ with $N_{sg}(e_i)$ number of sensors, the aforementioned steps can be generalized to obtain the updated design $e_{(i+1)}$.
2. The total number of sensors in the design reaches the maximum number of sensors limited/constrained by the decision-maker or other factors.

Given the design e_i, the updated design $e_{(i+1)}$ can be obtained following similar exercise as described above. Let $N_{\text{total}} = 64919 \times 4$ represent the total number of strain-gauges attached in the structure (at top and bottom of each 64919 elements in both vertical and horizontal direction). Let $e_{n_{\text{as}}}$ represent the optimized sensor design with $(N_0 + n_{\text{as}})$ sensors, such that $n_{\text{as}} \leqslant N_{\text{as}}$. Here, N_{as} represents the maximum additional sensors considered over the initially assumed number of sensors N_0. The number of sensors int final design shall then be $\leqslant (N_0 + N_{as})$.The optimal design e^* is then given by:

$$e^* = \text{argmax}_{e_{n_{\text{as}}}} \mathfrak{E}_{\text{implicit-risk}}(e_{n_{\text{as}}}). \tag{50}$$

The following Algorithm 1 demonstrates the Bayesian optimization procedure to evaluate the design e^*.

Algorithm 1: Bayesian optimization for sensor placement

Initialize $e_0 = \left(\mathscr{A}^{(1)}, \mathscr{A}^{(2)}, \cdots, \mathscr{A}^{(N_0)}\right)$;
for $n_{as} = 1$ **to** N_{as} **do**
  Using LHS, randomly select α locations to be candidates for the $(N_0 + n_{\text{as}})$ sensor location, with coordinates $\mathscr{X} = \left(\tilde{\mathscr{A}}^{(1)}, \tilde{\mathscr{A}}^{(2)}, \cdots, \tilde{\mathscr{A}}^{(\alpha)}\right)$;
  Obtain α number of possible designs: $\tilde{e}_k$ = concatenate $\left(e_{(n_{\text{as}}+1)}, \tilde{\mathscr{A}}^{(k)}\right)$, for all $k \leq \alpha$;
  Obtain the exact cost of all the α designs:
  $\Xi = \left(\mathfrak{E}_{\text{implicit-risk}}(\tilde{e}_1), \mathfrak{E}_{\text{implicit-risk}}(\tilde{e}_2), \cdots, \mathfrak{E}_{\text{implicit-risk}}(\tilde{e}_\alpha)\right)$;
  while $i = 1$ **or** $maxEI < \varepsilon$ **do**
    Construct the GPR model for $\hat{\mathfrak{E}}(\cdot)$ trained using $(\mathscr{X}, \Xi)$;
    For all the remaining strain locations $Z = \left(\bar{\mathscr{A}}^{(1)}, \bar{\mathscr{A}}^{(2)}, \cdots, \bar{\mathscr{A}}^{(\beta)}\right)$, where $\beta = \left(N_{\text{total}} - \left(N_0 + n_{\text{as}} - 1\right) - \alpha\right)$, obtain β number of possible designs:
    $\bar{e}_m$ = concatenate $\left(e_{(n_{\text{as}}+1)}, \bar{\mathscr{A}}^{(m)}\right)$, for all $m \leq \beta$;
    Obtain the cost $\hat{\mathfrak{E}}\left(\bar{\mathscr{A}}^{(m)}\right)$ for all $m \leq \beta$ designs using GPR developed before;
    Obtain the currrent best $\mathfrak{E}^* = \min \Xi$;
    Obtain the Expected Improvement for all the β designs using:

$$EI(\bar{\mathscr{A}}^{(m)}) = \left(\mu_{\bar{\mathscr{A}}^{(m)}} - \mathfrak{E}^*\right) \Phi\left(\frac{\mu_{\bar{\mathscr{A}}^{(m)}} - \mathfrak{E}^*}{\sigma_{\bar{\mathscr{A}}^{(m)}}}\right) + \sigma_{\bar{\mathscr{A}}^{(m)}} \phi\left(\frac{\mu_{\bar{\mathscr{A}}^{(m)}} - \mathfrak{E}^*}{\sigma_{\bar{\mathscr{A}}^{(m)}}}\right)$$

    , where $m \leq \beta$;
    Obtain:

$$maxEI = \max_{\bar{x}^{(m)}} \left(EI(\bar{\mathscr{A}}^{(m)})\right)$$
$$\bar{\mathscr{A}} = \arg\max_{\bar{x}^{(m)}} \left(EI(\bar{\mathscr{A}}^{(m)})\right)$$
$$\bar{e} = \text{concatenate}\left(e_{(n_{\text{as}}+1)}, \bar{\mathscr{A}}\right)$$

    Evaluate the exact cost $\mathfrak{E}_{\text{implicit-risk}}(\bar{e})$;
    Update:

$$\mathscr{X} = \text{concatenate}\left(\mathscr{X}, \bar{\mathscr{A}}\right)$$
$$\tilde{e}_{(\alpha+i)} = \bar{e}$$
$$\Xi = \text{concatenate}\left(\Xi, \mathfrak{E}_{\text{implicit-risk}}(\bar{e})\right)$$

    $i = i + 1$;
  end
  Update the sensor design: $e_{n_{\text{as}}} = \text{concatenate}(e_{n_{\text{as}}-1}, \bar{\mathscr{A}})$;
end
Obtain: $e^* = \arg\max_{e_k} \mathfrak{E}_{\text{implicit-risk}}(e_k)$, where, $k \leq N_{\text{as}}$;

5.2. Results and discussion

The initial design e_0 consisting of $N_0 \geqslant 0$ sensors may be randomly obtained via LHS, pre-defined based on judgment/-experience, or taken as 0 if no pre-defined design is available and if one does not want to assume a random initial design. We note in our case study that the miter gate finite element model is so finely meshed that there exists a spatial correlation between the strain values. Therefore, there are non-unique sensor locations that are sampled by the acquisition function, leading to non-unique and slightly different sensor designs depending on the different initial design e_0. In this paper, we numerically implement the optimization algorithm by fixing the initial design e_0 with $N_0 = 0$. Secondly, we consider $\theta_{\text{low}} = 70$inches, and $\theta_{\text{up}} = 180$inches. We reasonably assume the gap values below 70inches do not represent significant damage to the gate, and the gap value of 180inches represents the upper limit of the possible gap value beyond which the gate is considered to be critically damaged, based on discussions with USACE engineers. We perform the following studies:

1. In Section 5.2.1, we investigate and compare the capability of predicting the posterior distribution of the gap length using a random design consisting of 10 sensors (obtained using LHS) vs. optimal sensor design obtained using Bayes risk $\mathfrak{E}(e)$ that ignores the risk weight and considers KL divergence as the choice of f-divergence in the Bayes risk functional.
2. In Section 5.2.2, we investigate and compare the capability of a sensor design in predicting the posterior distribution of the gap length obtained using Bayesian optimization of Bayes risk functional constructed using various f-divergences, with and without the risk weighting. We consider 5 types of f-divergences in constructing the Bayes risk and compare their effectiveness in arriving at the optimal design.

5.2.1. Comparison of a optimal sensor placement design based on KL divergence (no risk weight) vs. randomly-chosen design

Fig. 13 illustrates the randomly chosen sensor design (left image), and the one arrived at by using KL divergence without risk weights in the Bayes risk functional (right image). We observe that all these sensors constituting the design obtained using KL divergence-based functional are concentrated close to the boundary of the quoin block and the gate. This location is desirable to capture the change in the strain values due to loss of contact between the quoin block and the gate (or for obtaining a better inference of the gap length), reflecting an unquestionable advantage of using Bayesian optimized sensor design over the randomly chosen design. It is also seen in Fig. 12, from the strain field plot obtained for a fixed set of loading parameters, that there is a stress concentration near the gap length that intuitively justifies the fact that optimal sensor design should contain at least a few sensors near the gap. Secondly, from Fig. 14, we observe that sensor placement optimization significantly increases the effectiveness of Bayesian inference. This leads to a significant reduction in the uncertainty associated with the posterior distribution of the gap length for different realizations of the true gap values. Thirdly, as seen in Fig. 14b, the uncertainty in the posterior distribution is not equally/uniformly reduced for different realizations of true gap length. This is because the obtained optimal sensor design can reduce more uncertainty for certain true gap lengths and less for the other ones. Despite this local non-uniformity, the sensor design obtained using Bayesian optimization is optimal in a global sense.

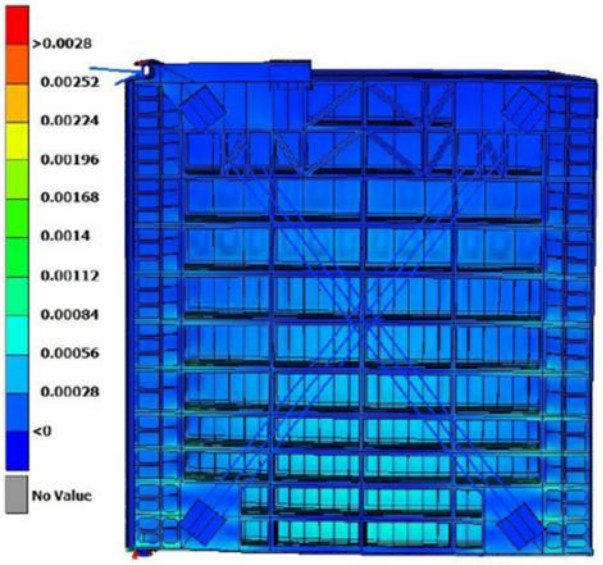

Fig. 12. Stress field plot of the miter gate structure obtained for a fixed set of load parameters.

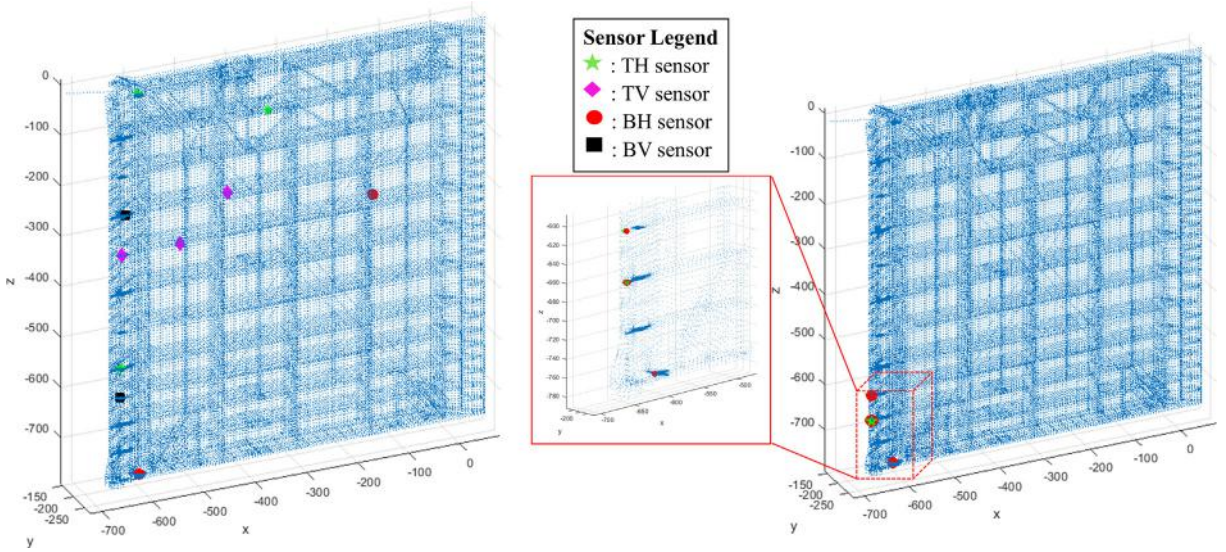

Fig. 13. Randomly chosen 10 sensor design (left) vs. KL divergence optimized (no risk weight) 10 sensor design (right).

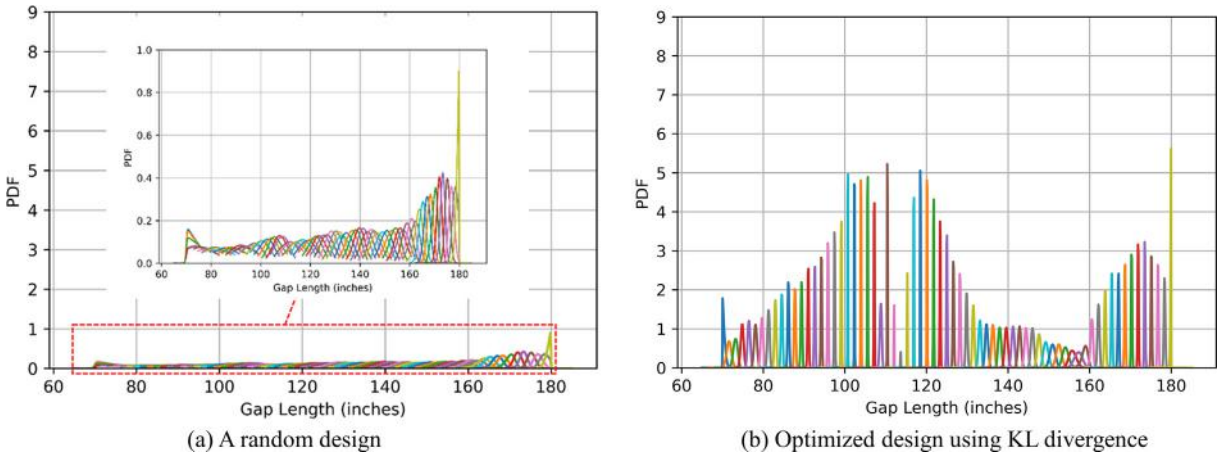

Fig. 14. Posterior distributions obtained using a randomly chosen 10 sensor design vs. KL divergence (no risk weight) optimized 10 sensor design.

5.2.2. Comparison of an optimal sensor placement design obtained using f-divergence with risk weights vs. without risk weights

In this section, we compare the effectiveness of sensor design in Bayesian inference obtained using different kinds of *f*-divergences with and without the risk weight. We consider the 5 different *f*-divergences: KL, Hellinger, total variation, Pearson, and Jensen divergence. The following subsections illustrate a set of three plots for each of the *f*-divergence considered:

1. Figs. 15,18,21,24,27, illustrates the sensor design arrived by ignoring the risk weights (left figure), and by including the risk weights (right figure) in Bayes risk functional.
2. Figs. 16,19,22,25,28, illustrates the posterior distribution of the gap length arrived for different realizations of the true gap length values by ignoring the risk weight (left figure) and by including the risk weights (right figure).
3. Figs. 17,20,23,26,29, illustrates the ratio of the maximum value of the posterior distribution of the gap length with and without the risk weights (left figure), and the ratio of the standard deviation of the posterior distribution of the gap length with and without the risk weights (right figure) for different realizations of the true gap length values.

First, we recall that one of the criteria for the Bayes risk functional was to incorporate our desire to obtain better information/description of the gap length when the true value of gap length is larger or when the state of the structure approaches a higher degree of damage. As is seen in Figs. 16,19,22,25,28, the optimization using risk-weighted (implicit) Bayes risk functional allows us to have higher confidence in the inference results for larger value of true gap length (or for higher degree of damage). However, accomplishing better inference at a higher value of the true gap length leads to

sacrifice in the performance of the Bayesian optimization at a lower value of the true gap length. This fact is reflected in Figs. 17a, 20a, 23a, 26a, and 29a, such that the ratio of the maximum value of the posterior with or without risk weight is higher at larger value of true gap length. Similarly, as seen in Figs. 17b, 20b, 23b, 26b, and 29b, the ratio of the standard deviation of the posterior with or without risk weight is lower at larger value of true gap length. Second, the majority of the sensors identified are in the horizontal direction (TH and BH), and only a few are in the vertical direction (TV and BV). Third, the optimization results are dependent on the choice of *f*-divergence.

As observed in Fig. 15 for the risk-weighted KL divergence case (right figure) that one sensor (highlighted by a red circle) is far away from the gap (unlike the other sensors that are close to the gap). This is counter-intuitive and deserves an explanation. The algorithm searches the global domain for the *next possible candidate*. There are two possibilities of such selection:

1. The outlier (for example: BV sensor circled in red in Fig. 15) could have been selected in the initial iteration steps. It would have been an incorrect choice that the algorithm would self-correct by picking appropriate sensors in the next iterations.
2. The outlier (for example: BV sensor circled in red in Fig. 15) was selected in the later iteration step (closer to the converging point). In that case, the information provided by the sensors selected in the preceding iteration steps was enough to capture the required information and the BV sensor did not add much value to the design. This was the case in selecting the BV sensor in Fig. 15 highlighted by red circle.

Since the algorithm searches the entire space (global search), it may have been duped by the resembling and related strain information at different coordinates. However, the self-correcting nature of the algorithm would eventually select a combination of sensors (in the final design) that would capture the necessary information.

For the case of optimization where risk-weights are ignored, it is observed from Figs. 16a, 19a,22a, 25a, and 28a, that at true gap length in the neighborhood of 110 inches, the posterior distribution of the gap length has higher variability than the distributions at other gap values slightly higher or lower to 110 inches. It can be seen with a closer look that there are some senors near the 110 inches gap value in the final design (see the green circle highlighted portion of the left part of Fig. 15). These sensors may be relatively more sensitive to the gap value lower or higher than 110 inches partly because of their location and the component of the gate they are attached to (a gate is a complex structure consisting of many elements welded together). Although these sensors may not be as sensitive to 110 inches gap degradation, they certainly are sensitive to other gap values. Since the optimization framework presented in this paper chooses the optimal design in an average sense, the relative advantage (optimal sensitivity to the overall damaged state) of these sensors is one possible reason for them to be picked by the optimization algorithm in the first place.

5.3. Comparison of an optimal sensor placement design obtained using KL divergence with vs. without risk weight

Figs. 15,16,17.

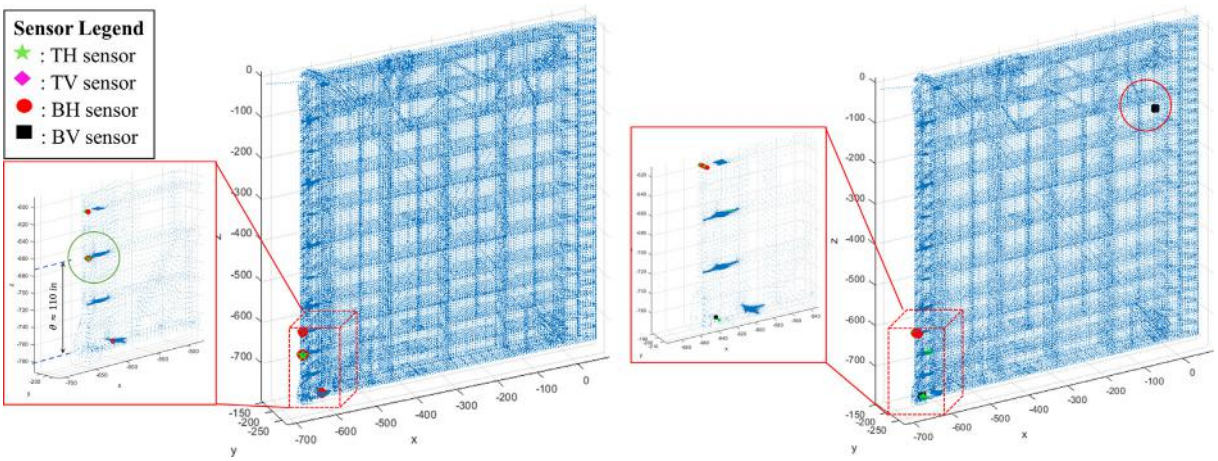

Fig. 15. Sensor placement design using KL divergence: without (left) and with (right) the risk weight.

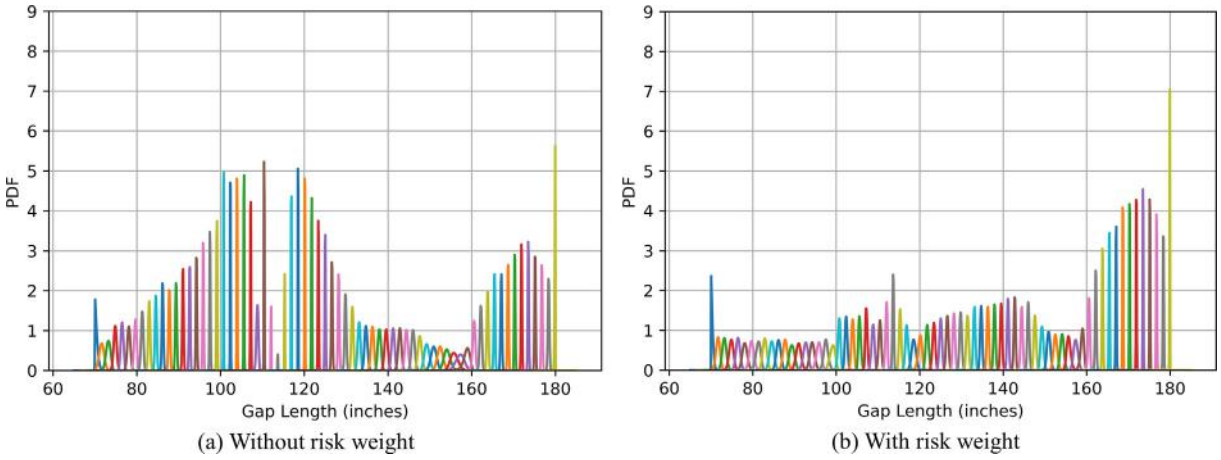

Fig. 16. Posterior distributions obtained using KL divergence.

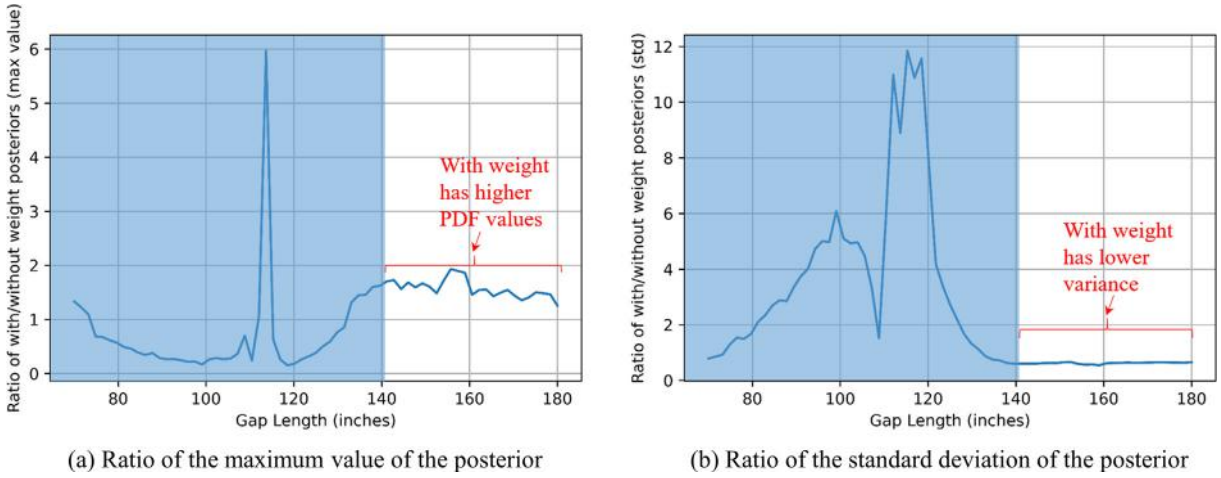

Fig. 17. Ratio of the maximum value and the standard deviation of the posterior obtained using KL divergence with and without risk weight.

5.3.1. Comparison of an optimal sensor placement design obtained using Hellinger divergence with vs. without risk weight

Figs. 18,19,20.

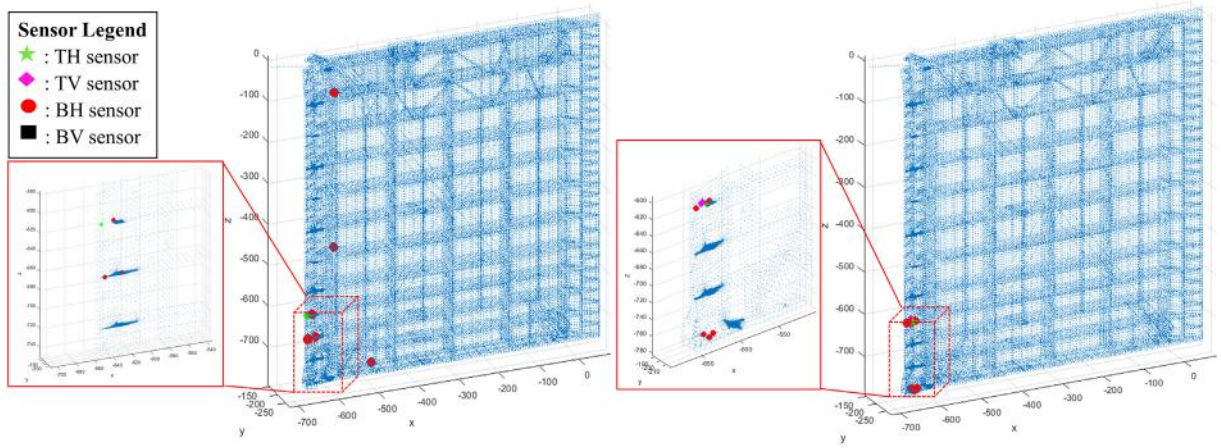

Fig. 18. Sensor placement design using Hellinger divergence: without (left) and with (right) the risk weight.

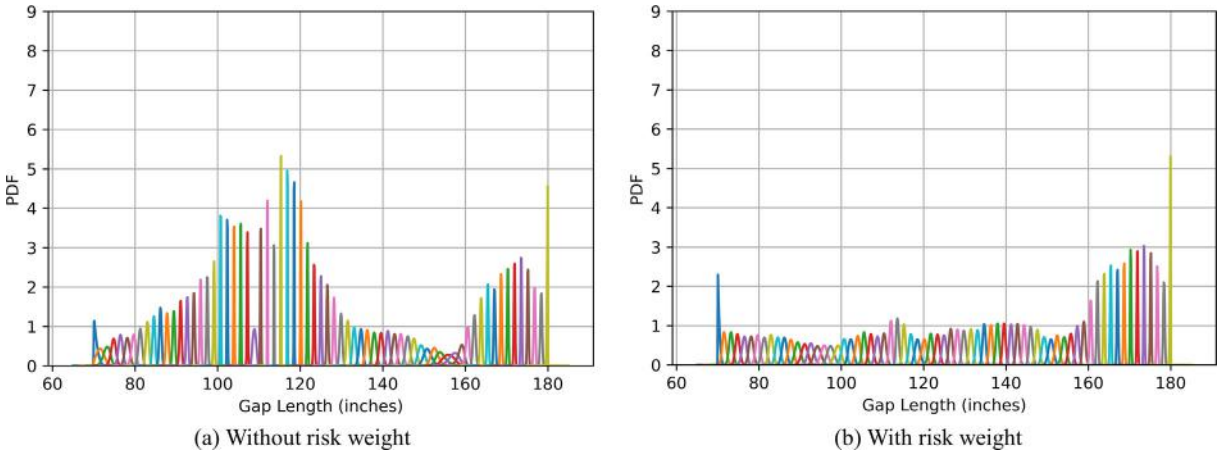

Fig. 19. Posterior distributions obtained using Hellinger divergence.

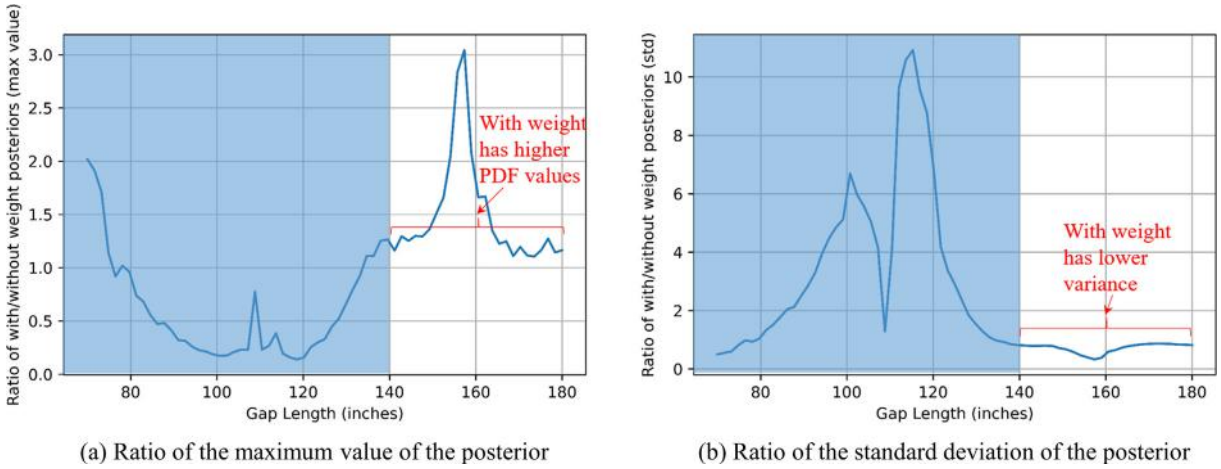

Fig. 20. Ratio of the maximum value and the standard deviation of the posterior obtained using Hellinger divergence with and without risk weight.

5.3.2. Comparison of an optimal sensor placement design obtained using total variation f-divergence with vs. without risk weight

Figs. 21,22,23.

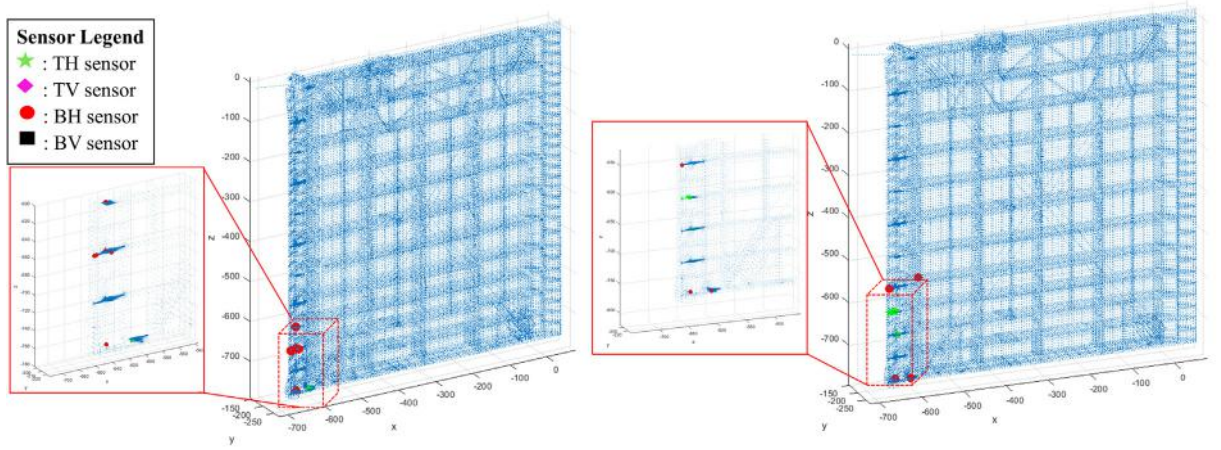

Fig. 21. Sensor placement design using total variation *f*-divergence: without (left) and with (right) the risk weight.

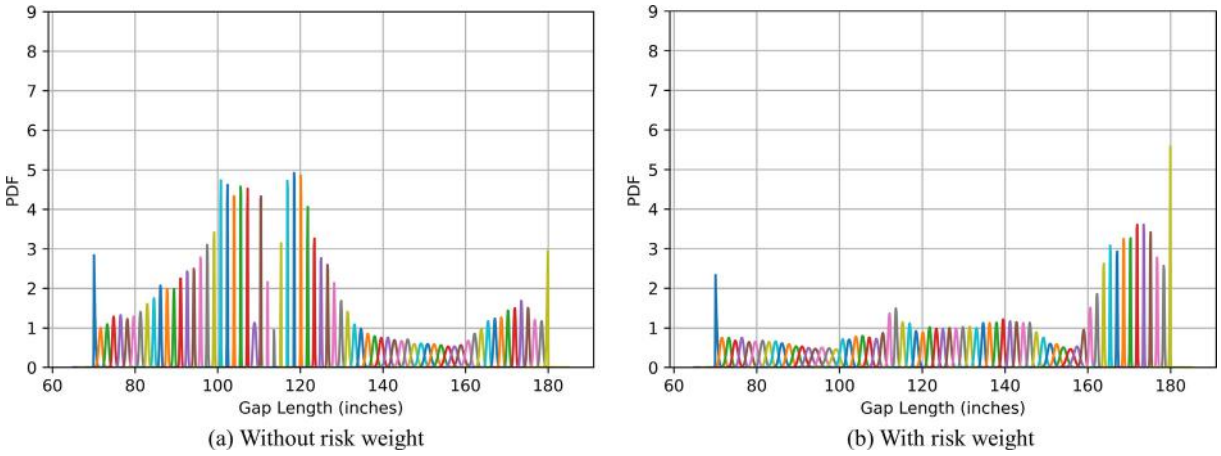

Fig. 22. Posterior distributions obtained using total variation *f*-divergence.

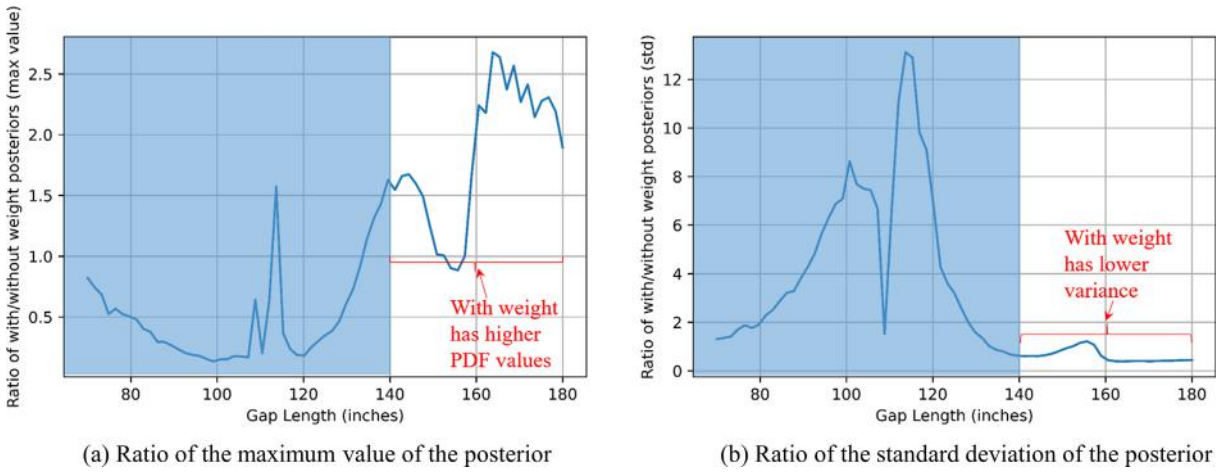

Fig. 23. Ratio of the maximum value and the standard deviation of the posterior obtained using total variation *f*-divergence with weight and without weight.

5.3.3. Comparison of an optimal sensor placement design obtained using Pearson f-divergence with vs. without risk weight

Figs. 24,25,26.

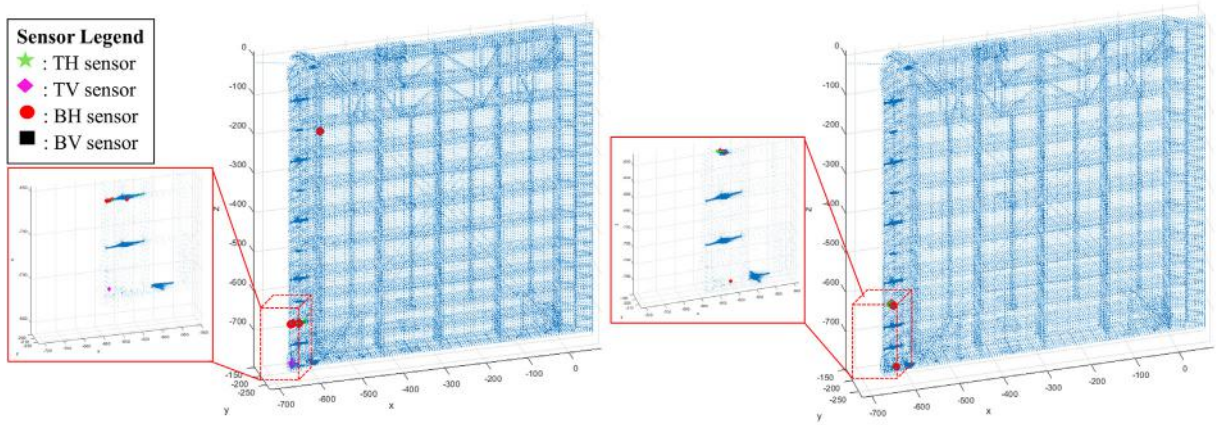

Fig. 24. Sensor placement design using Pearson *f*-divergence: without (left) and with (right) the risk weight.

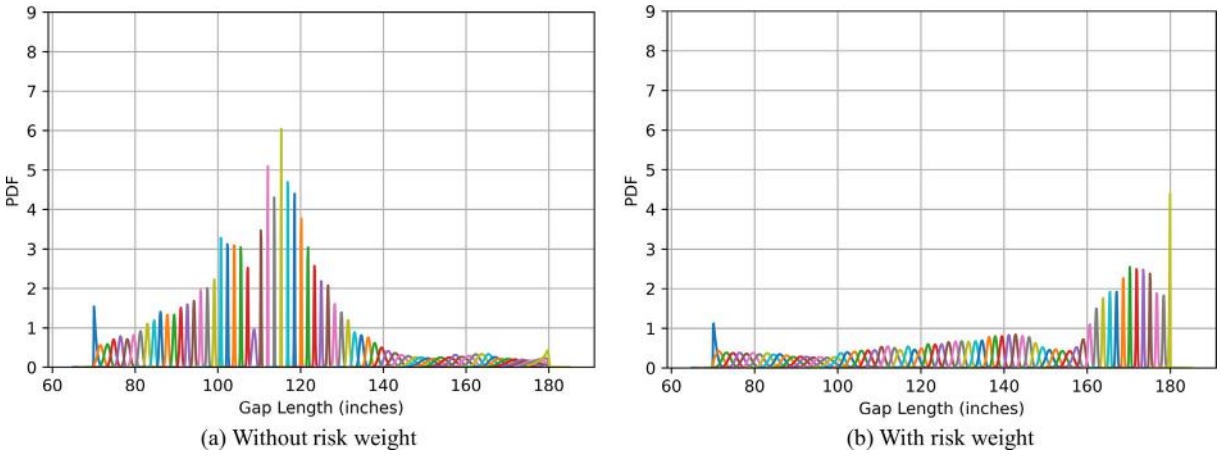

Fig. 25. Posterior distributions obtained using Pearson *f*-divergence.

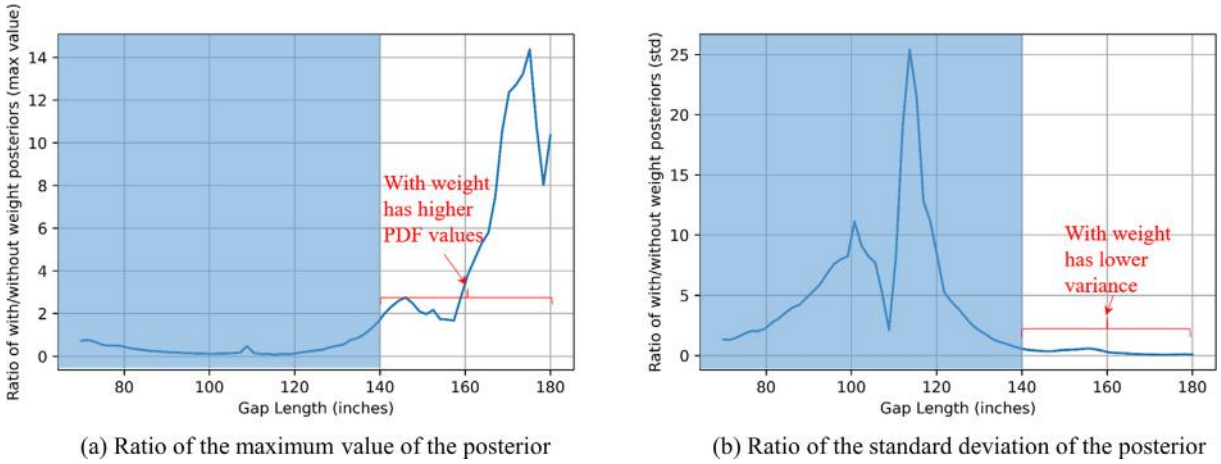

Fig. 26. Ratio of the maximum value and the standard deviation of the posterior obtained using Pearson *f*-divergence with and without risk weight.

5.3.4. Comparison of an optimal sensor placement design obtained using Jensen f-divergence with vs. without risk weight

Figs. 27,28,29.

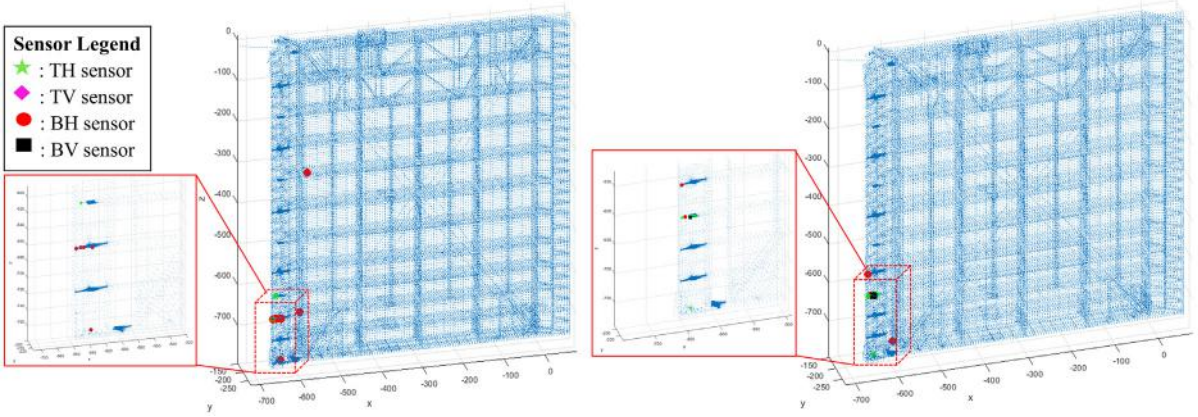

Fig. 27. Sensor placement design using Jensen *f*-divergence: without (left) and with (right) the risk weight.

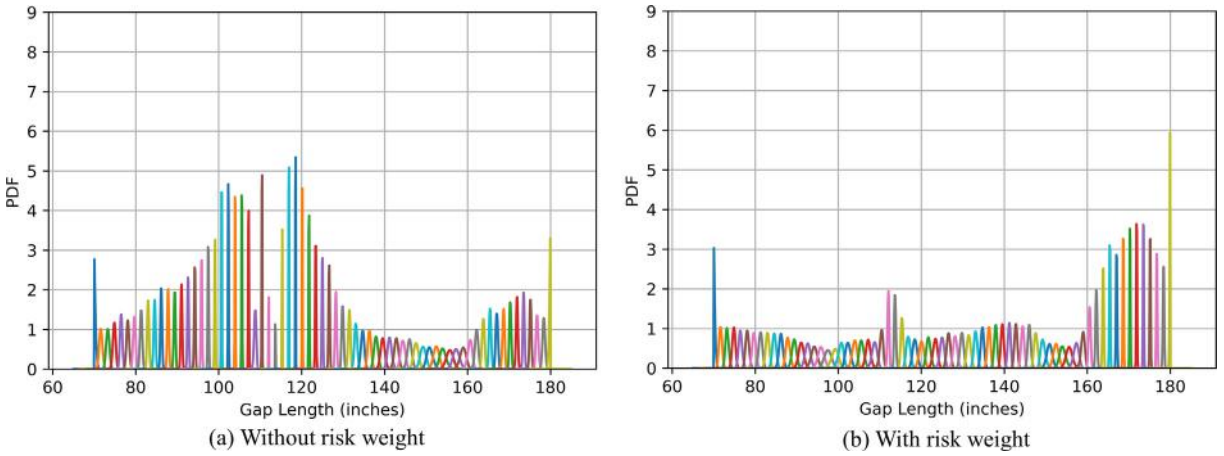

Fig. 28. Posterior distributions obtained using Jensen *f*-divergence.

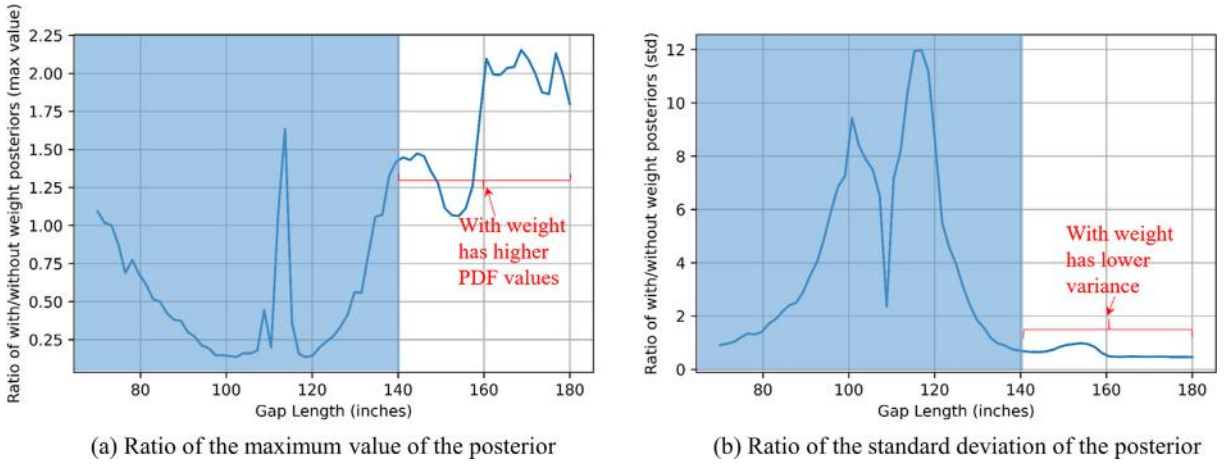

Fig. 29. Ratio of the maximum value and the standard deviation of the posterior obtained using Jensen *f*-divergence with and without weight.

5.3.5. Comparison of an optimal sensor placement design obtained using different f-divergences relative to KL divergence with and without risk weight

Fig. 30a illustrates the ratio of the standard deviation of the posterior distribution of the gap length obtained by various *f-divergences without risk weight* with respect to the standard deviation obtained using *KL divergence without risk weight*. Similarly, Fig. 30b represents the same ratio when risk weights are considered in the Bayes risk functional.

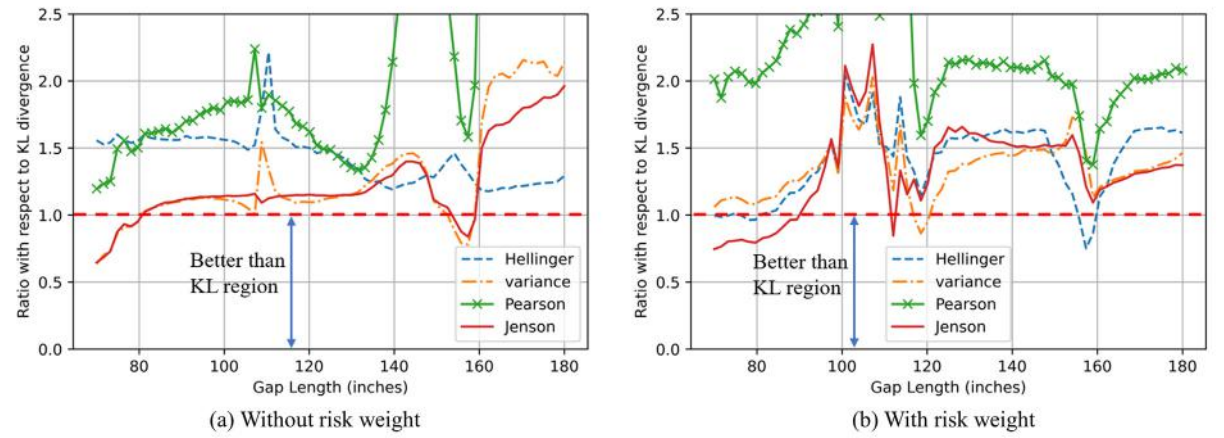

Fig. 30. Ratio of the standard deviation of the posterior obtained using various *f*-divergence relative to the standard-deviation obtained using KL divergence.

We observe that among the *f*-divergences studied for the application of optimal sensor design, Bayes risk functional considering KL divergence leads to the best sensor placement design for both with or without risk weights.

6. Summary and conclusions

This paper details an optimal sensor design framework for structural health monitoring applications. It was demonstrated on a miter gate case study with the primary goal of arriving at the optimal strain gauge network design used to infer the posterior distribution of the loss-in-contact gap length (the damage state parameter). We arrived at such a design by maximizing an objective functional referred to as *Bayes risk*. The Bayes risk is designed to accommodate three crucial elements: first, it aims to obtain a design that maximizes the gains in the information on the gap length inferred from the strain-gauge measurements. This gain in the information is quantified by *f-divergence* that evaluates the similarity or dissimilarity between two probability measures by evaluating the distance (relative gain of information) between two distributions. Second, the Bayes risk incorporates our desire to obtain better information/description of the gap length when the true value of gap length is larger or the state of the structure approaches a higher degree of damage. It is crucial for deciding the maintenance strategies and appropriate action preventing significant losses. It is accomplished by using a *risk-weight*. Third, the Bayes risk also takes into account our *prior knowledge* of the gap length.

Arriving at the optimal sensing design was accomplished by minimizing risk or equivalently maximizing the utility (defined as the risk-weighted gain of information) in an *average* sense. In this regard, evaluation of the Bayes risk for a given sensor network design demands considering all the possible degrees of damage (indicated by the true gap length value). This requires obtaining a large set of *simulated observation data* and a quick *Bayesian inference* of the posterior distribution of gap length for many different realizations of the true gap length values. Given a true gap length value and the loading parameters, the simulated strain gauge readings can be obtained using a high-fidelity finite element model (FEM). The randomness in the strain measurements is primarily due to uncertainties in the hydrostatic load parameters, and the noise in strain gauges. Since the high fidelity finite element model is computationally expensive, we built a digital surrogate using Gaussian Process Regression (GPR), which is around 50000 times faster than FEM. We deploy numerical approximation of the posterior distribution by using particle filters, or specifically the sequential Monte Carlo (SMC) approach. We define two approaches, intrinsic and extrinsic, to incorporate risk weights into Bayes risk functional. Although both, the intrinsic and extrinsic, definitions of Bayes risk are mathematically equivalent, the numerical evaluation of the intrinsic and extrinsic Bayes risk functional yields slightly different results. We use implicit Bayes risk because it shows the effect of risk weights more prominently than the result obtained using the explicit form of Bayes risk. Numerically evaluating Bayes risk expression involves evaluating a non-linear, multi-dimensional integral. We use univariate dimension reduction in conjuncture with the Gauss-Hermite quadrature. Apart from reducing the computational cost by using GPR, we also proposed a novel and innovative approach to further minimize the computational cost for evaluating the Bayes risk by minimizing the number of times we run the GPR model to evaluate the Bayes risk.

We observe that as compared to random sensor design, the optimal sensor design significantly increases the effectiveness of Bayesian inference and reduces the uncertainty in the posterior distribution of the gap length value. Inclusion of the risk-weight in Bayes risk allows us to have higher confidence in the inference results for a higher degree of damage (as was intended). However, accomplishing better inference at a higher value of the true gap length leads to sacrifice in the performance of the Bayesian optimization at a lower value of the true gap length. Amongst the chosen *f*-divergences, we conclude that KL divergence is the most suitable choice for this particular class of problems. A future possible work can be to compare the efficiency and results obtained by the presented Bayesian optimization with other algorithms in the literature for the given problem. The computational speed, as well as the final design, arrived using various optimization algorithms may depend on how the algorithm is engineered, and the constraints on the problem at hand, and it remains to be investigated.

CRediT authorship contribution statement

Yichao Yang: Formal analysis, Writing - original draft. **Mayank Chadha:** Conceptualization, Methodology, Formal analysis, Writing - original draft. **Zhen Hu:** Conceptualization, Formal analysis, Methodology, Writing - original draft, Writing - review & editing. **Manuel A. Vega:** Methodology, Formal analysis, Writing - original draft, Writing - review & editing. **Matthew D. Parno:** Methodology, Writing - review & editing. **Michael D. Todd:** Conceptualization, Funding acquisition, Project administration, Supervision, Writing - review & editing.

Declaration of Competing Interest

The authors declare that they have no known competing financial interests or personal relationships that could have appeared to influence the work reported in this paper.

Acknowledgment

Funding for this work was provided by the United States Army Corps of Engineers through the U.S. Army Engineer Research and Development Center Research Cooperative Agreement W912HZ-17–2-0024.

Appendix A

A.1. Various types of f-divergences

Table 1

References

[1] S. Thöns, M.H. Faber, Assessing the value of structural health monitoring, ICOSSAR'13 – 11th International Conference on Structural Safety and Reliability – Safety, Reliability, Risk and Life-cycle Performance of Structures and Infrastructures (Proceedings), 2013..
[2] V. Akbarzadeh, J.-C. Lévesque, C. Gagné, M. Parizeau, Efficient sensor placement optimization using gradient descent and probabilistic coverage, Sensors 14 (8) (2014) 15525–15552.
[3] M. Parno, D. O'Connor, M. Smith, High dimensional inference for the structural health monitoring of lock gates, arXiv preprint arXiv:1812.05529, 2018..
[4] D.C. Kammer, Sensor placement for on-orbit modal identification and correlation of large space structures, J. Guidance Control Dyn. 14 (2) (1991) 251–259.
[5] D.C. Kammer, Optimal sensor placement for modal identification using system-realization methods, J. Guidance Control Dyn. 19 (3) (1996) 729–731.
[6] Z. Shi, S. Law, L. Zhang, Optimum sensor placement for structuraldamage detection, J. Eng. Mech. 126 (11) (2000) 1173–1179.
[7] L. Yao, W.A. Sethares, D.C. Kammer, Sensor placement for on-orbit modal identification via a genetic algorithm, AIAA J. 31 (10) (1993) 1922–1928.
[8] G.F. Gomes, F.A. de Almeida, P. d. S.L. Alexandrino, S.S. da Cunha, B.S. de Sousa, A.C. Ancelotti, A multiobjective sensor placement optimization for shm systems considering fisher information matrix and mode shape interpolation, Eng. Comput. 35 (2) (2019) 519–535.
[9] H. Sun, O. Büyüköztürk, Optimal sensor placement in structural health monitoring using discrete optimization, Smart Mater. Struct. 24 (12) (2015) 125034.
[10] A. Downey, C. Hu, S. Laflamme, Optimal sensor placement within a hybrid dense sensor network using an adaptive genetic algorithm with learning gene pool, Struct. Health Monitor. 17 (3) (2018) 450–460.
[11] C. Papadimitriou, J.L. Beck, S.-K. Au, Entropy-based optimal sensor location for structural model updating, J. Vib. Control 6 (5) (2000) 781–800.
[12] F. Unwadia, Methodology for optimal sensor locations for parameter identification in dynamic system, J. Eng. Mech. 120 (1994) 368–390.
[13] M. Basseville, A. Benveniste, G. Moustakides, A. Rougee, Optimal sensor location for detecting changes in dynamical behavior, IEEE Trans. Autom. Control 32 (12) (1987) 1067–1075.
[14] W.A. Maul, G. Kopasakis, L.M. Santi, T.S. Sowers, A. Chicatelli, Sensor selection and optimization for health assessment of aerospace systems, J. Aerosp. Comput. Inf. Commun. 5 (1) (2008) 16–34.
[15] E. Peh, Y.-C. Liang, Optimization for cooperative sensing in cognitive radio networks, in: 2007 IEEE Wireless Communications and Networking Conference, IEEE, 2007, pp. 27–32.
[16] R.F. Guratzsch, S. Mahadevan, Structural health monitoring sensor placement optimization under uncertainty, AIAA J. 48 (7) (2010) 1281–1289.
[17] E. Chan, Optimal design of building structures using genetic algorithms, California Institute of Technology, Report No. EERL 97-06, 1997..
[18] T.-H. Yi, H.-N. Li, M. Gu, A new method for optimal selection of sensor location on a high-rise building using simplified finite element model, Struct. Eng. Mech. 37 (6) (2011) 671–684.
[19] S.R. Peddada, P.J. Tannous, A.G. Alleyne, J.T. Allison, Optimal sensor placement methods in active high power density electronic systems with experimental validation, J. Mech. Design 142 (2) (2020)..
[20] E.B. Flynn, M.D. Todd, A bayesian approach to optimal sensor placement for structural health monitoring with application to active sensing, Mech. Syst. Signal Process. 24 (4) (2010) 891–903.
[21] M.D. Todd, E.B. Flynn, A bayesian experimental design approach for structural health monitoring, in: Proceedings of the XIV International Symposium on Dynamic Problems of Mechanics (DINAME 2011), Brazil, 2011..
[22] F. Chaloner, I. Verdinelli, Bayesian experimental design: a review, Stat. Sci. 10 (3) (1995) 273–304.
[23] B. Li, A. Der Kiureghian, Robust optimal sensor placement for operational modal analysis based on maximum expected utility, Mech. Syst. Signal Process. 75 (2016) 155–175.
[24] C. Argyris, S. Chowdhury, V. Zabel, C. Papadimitriou, Bayesian optimal sensor placement for crack identification in structures using strain measurements, Struct. Control Health Monitor. 25 (5) (2018) e2137.
[25] Z. Hu, D. Ao, S. Mahadevan, Calibration experimental design considering field response and model uncertainty, Comput. Methods Appl. Mech. Eng. 318 (2017) 92–119.
[26] L. Bottou, Large-scale machine learning with stochastic gradient descent, in: Proceedings of COMPSTAT'2010, Springer, 2010, pp. 177–186.
[27] S.S. Ram, A. Nedic, V.V. Veeravalli, Stochastic incremental gradient descent for estimation in sensor networks, in: 2007 Conference Record of the Forty-First Asilomar Conference on Signals, Systems and Computers, IEEE, 2007, pp. 582–586.
[28] S. Jin, M. Zhou, A.S. Wu, Sensor network optimization using a genetic algorithm, in: Proceedings of the 7th World Multiconference on Systemics, Cybernetics and Informatics, 2003, pp. 109–116..
[29] T.-H. Yi, H.-N. Li, M. Gu, Optimal sensor placement for health monitoring of high-rise structure based on genetic algorithm, Math. Probl. Eng. 2011 (2011).
[30] Z. Hu, S. Nannapaneni, S. Mahadevan, Efficient kriging surrogate modeling approach for system reliability analysis, AI EDAM 31 (2) (2017) 143–160.
[31] P. Nath, Z. Hu, S. Mahadevan, Sensor placement for calibration of spatially varying model parameters, J. Comput. Phys. 343 (2017) 150–169.
[32] S. Rahman, H. Xu, A univariate dimension-reduction method for multi-dimensional integration in stochastic mechanics, Probab. Eng. Mech. 19 (4) (2004) 393–408.
[33] D.R. Jones, M. Schonlau, W.J. Welch, Efficient global optimization of expensive black-box functions, J. Global Optim. 13 (4) (1998) 455–492.
[34] P.I. Frazier, A tutorial on bayesian optimization, 2018.
[35] T.-H. Yi, H.-N. Li, Methodology developments in sensor placement for health monitoring of civil infrastructures, Int. J. Distrib. Sens. Netw. 8 (8) (2012) 612726.
[36] W. Ostachowicz, R. Soman, P. Malinowski, Optimization of sensor placement for structural health monitoring: a review, Struct. Health Monitor. 18 (3) (2019) 963–988.
[37] Y. Tan, L. Zhang, Computational methodologies for optimal sensor placement in structural health monitoring: a review, Struct. Health Monitor. 19 (4) (2020) 1287–1308.
[38] J.P. Schwieterman, S. Field, L. Fischer, A. Pizzano, An Analysis of the Economic Effects of Terminating Operations at the Chicago River Controlling Works and O'brien Locks on the Chicago Area Waterway System, DePaul University, Chicago, IL, 2010.
[39] S.D. Foltz, Investigation of mechanical breakdowns leading to lock closures, tech. rep., ERDC-CERL CHAMPAIGN United States, 2017..
[40] B.A. Eick, Z.R. Treece, B.F. Spencer Jr, M.D. Smith, S.C. Sweeney, Q.G. Alexander, S.D. Foltz, Automated damage detection in miter gates of navigation locks, Struct. Control Health Monitor. 25 (1) (2018) e2053.
[41] M.A. Vega, M.D. Todd, A variational bayesian neural network for structural health monitoring and cost-informed decision-making in miter gates, Struct. Health Monitor. (2020)1475921720904543..
[42] M. Chadha, M.D. Todd, A comprehensive kinematic model of single-manifold cosserat beam structures with application to a finite strain measurement model for strain gauges, Int. J. Solids Struct. 159 (2019) 58–76.

[43] S.L. Padula, R.K. Kincaid, Optimization strategies for sensor and actuator placement, NASA/TM-1999-209126, 1999..
[44] C. Malings, M. Pozzi, Optimal sensor placement and scheduling with value of information for spatio-temporal infrastructure system management, in: Proc., 12th Int. Conf. on Structural Safety and Reliability, 2017, pp. 3320–3330..
[45] B.A. Eick, M.D. Smith, T.B. Fillmore, Feasibility of retrofitting existing miter-type lock gates with discontinuous contact blocks, J. Struct. Integr. Maintenance 4 (4) (2019) 179–194.
[46] M. Moustapha, J.-M. Bourinet, B. Guillaume, B. Sudret, Comparative study of kriging and support vector regression for structural engineering applications, ASCE-ASME J. Risk Uncertain. Eng. Syst. A: Civil Eng. 4 (2) (2018) 04018005.
[47] L. Yu, S. Wang, K.K. Lai, A neural-network-based nonlinear metamodeling approach to financial time series forecasting, Appl. Soft Comput. 9 (2) (2009) 563–574.
[48] G. Capellari, E. Chatzi, S. Mariani, Cost–benefit optimization of structural health monitoring sensor networks, Sensors 18 (7) (2018) 2174.
[49] S. Lloyd, Measures of complexity: a nonexhaustive list, IEEE Control Syst. Mag. 21 (4) (2001) 7–8.
[50] J. Mockus, V. Tiesis, A. Zilinskas, The application of bayesian methods for seeking the extremum, Towards Global Optim. 2 (2) (1978) 117–129.
[51] D.R. Jones, M. Schonlau, W.J. Welch, Efficient global optimization of expensive black-box functions, J. Global Optim. 13 (4) (1998) 455–492.
[52] D.V. Lindley, On a measure of the information provided by an experiment, Ann. Math. Stat. (1956) 986–1005..
[53] X. Huan, Y.M. Marzouk, Simulation-based optimal bayesian experimental design for nonlinear systems, J. Comput. Phys. 232 (1) (2013) 288–317.
[54] I. Csiszár and P.C. Shields, Information theory and statistics: A tutorial. Now Publishers Inc, 2004..
[55] I. Sason, S. Verdu, f-divergence inequalities, IEEE Trans. Inf. Theory 62 (11) (2016) 5973–6006.
[56] F. Nielsen, R. Nock, On the chi square and higher-order chi distances for approximating f-divergences, IEEE Signal Process. Lett. 21 (1) (2013) 10–13.
[57] F. Osterreicher, I. Vajda, A new class of metric divergences on probability spaces and its applicability in statistics, Ann. Inst. Stat. Math. 55 (3) (2003) 639–653.
[58] M. Khosravifard, D. Fooladivanda, T.A. Gulliver, Confliction of the convexity and metric properties in f-divergences, IEICE Trans. Fundam. Electron., Commun. Comput. Sci. 90 (9) (2007) 1848–1853.
[59] X. Nguyen, M.J. Wainwright, M.I. Jordan, Estimating divergence functionals and the likelihood ratio by penalized convex risk minimization, in: Advances in Neural Information Processing Systems, 2008, pp. 1089–1096..
[60] P. Rubenstein, O. Bousquet, J. Djolonga, C. Riquelme, I.O. Tolstikhin, Practical and consistent estimation of f-divergences, in: Advances in Neural Information Processing Systems, 2019, pp. 4072–4082..